https://doi.org/10.5194/egusphere-2026-2212
Preprint. Discussion started: 15 June 2026

Frequent new particle formation events in the Indo-Gangetic Plain occur under reduced condensation sink but are obscured by air mass heterogeneity

Gaurav K. Srivastav[1,2], Aasif A. Wagay[1], Janne Lampilahti[3], Jaswant Rathore[1], Ravi K. Kunchala[1], Dilip Ganguly[1], Markku Kulmala[3], Tuukka Petäjä[3], Pauli Paasonen[3], Roseline C. Thakur[3*], Shahzad Gani[1,3*]

[1]Centre for Atmospheric Sciences, Indian Institute of Technology Delhi, New Delhi, India.
[2]India Meteorological Department, Ministry of Earth Sciences, Government of India.
[3]Institute for Atmospheric and Earth System Research/Physics, University of Helsinki, Helsinki, Finland.

Correspondence to: shahzadgani@iitd.ac.in; roseline.thakur@helsinki.fi

Abstract. New particle formation (NPF) is a major source of atmospheric aerosols and cloud condensation nuclei, influencing climate and air quality. In highly polluted regions such as the Indo-Gangetic Plain (IGP), where precursor concentrations and condensation sinks are among the highest globally, NPF remains poorly constrained due to limited observations of particles and ions in sub–10 nm size range.

Here, we investigated the occurrence and microphysical evolution of NPF at a suburban IGP site (CAS-AO, Sonipat, Haryana), during May – December 2023 using ion and particle measurements together with meteorological data. NPF events are frequent during summer and less common in winter. The weak seasonal variability of ion concentrations relative to nucleation-mode particles suggests that neutral pathways dominate NPF in this high-sink environment. The median condensation sinks on event-days (0.024 s^{-1}) are approximately half those on non-event days (0.046 s^{-1}). Particle growth rates (maximum concentration method) increase with size, from 14.7 nm h^{-1} (3–7 nm) to 19.0 nm h^{-1} (7–20 nm), indicating size-dependent condensational growth.

In this high-background setting, pollution plumes, and meteorological variability intermittently mask or distort NPF signals, limiting the direct applicability of both visual and automated classification methods and growth rate estimation methods. Our observations highlight that careful application and improvement of data analysis methods, along with precursor gas measurements, are required to better constrain nucleation processes by avoiding methodological sensitivity due to the complexity of aerosol dynamic processes in multi-source, high-condensation-sink environments, such as IGP.

1. Introduction

Aerosols affect the global radiation balance by scattering sunlight and altering cloud properties. They originate from natural (e.g., volcanoes, sea spray) and human sources (e.g., industry, transport) and occur as primary (directly emitted) or secondary (formed via atmospheric reactions) particles (Hinds and Zhu, 2022). Aerosol sizes range from a sub 2nm, comprising atmospheric clusters (particles) and small ions, to coarse particles reaching even hundreds of micrometres (Kulmala et al., 2024; Tomasi and Lupi, 2017). Particles originating from NPF, typically appear first as freshly nucleated particles with diameters of about 1.5–2 nm. Other sources for this range are transportation and combustion processes. Atmospheric observations and model results show that NPF followed by subsequent growth, contributes 10–60 % (with 38–66 % uncertainty; Gordon et al., 2017) to total aerosol particle number or cloud condensation nuclei (CCN) concentrations, particularly on NPF event-days (Kerminen et al., 2018; Sebastian et al., 2022).

At the nanoscale level, due to molecular aggregates carrying electric charge, some aerosols exist in an ionised state and significantly influence the atmospheric electrical properties (Seinfeld and Pandis, 2016). These particles are known as atmospheric ions and are typically generated through processes such as cosmic rays, radioactive decay, and lightning (Bazilevskaya et al., 2008; Eisenbud and Gesell, 1997; Mironova et al., 2015). The charge of these ionised particles is lost through processes such as ion–ion recombination, contact with surfaces, or can be transferred to other uncharged aerosol particles (Seinfeld and Pandis, 2016; Tammet, 1995). Their concentration varies with altitude, latitude, and meteorological conditions. They play role in various atmospheric processes, including new particle formation (NPF), further growth of formed particles, cloud formation, atmospheric electricity, and climate change (Boy et al., 2008; Carslaw et al., 2002; Kirkby et al., 2016; Kulmala et al., 2004; Laakso, 2003).

The Indo-Gangetic Plain (IGP), spanning parts of India, Pakistan, Bangladesh, and Nepal, supports intensive agriculture through its fertile alluvial soil and major river systems. It is a densely populated region characterized by complex meteorological factors, and faces pressing challenges related to rapid urbanization and industrial growth, resulting in significant air pollution levels. The region not only witnesses extreme levels of air pollution in winters but also experiences anomalies in precipitation, alternating weather during the Indian summer monsoon period and periodic impact of western disturbances. IGP, characterized by a rich mix of industrial and anthropogenic activities, presents a diverse array of aerosol sources. Increasing aerosol loading, along with a prominent role of precursors such as NH_3 (primarily from agricultural emissions), and discernible upward trend in SO_2 and NO_x are likely to enhance the potential for secondary aerosol formation and further complicate atmospheric processes (Chutia et al., 2022; Gani et al., 2019; Pawar et al., 2023; Singh et al., 2023; Wang et al., 2020). However, current knowledge of these processes in the IGP remains limited because previous studies have largely relied on the Scanning Mobility Particle Sizer (SMPS) and similar instruments optimized for higher diameter size ranges (typically above 10 nm), which often miss the critical dynamics of clusters below 3–10 nm (Kanawade et al., 2022). Furthermore, many existing observations are conducted over short time durations, making it difficult to fully understand the region's significant seasonal contrasts. These factors stress the need to study the nuances of secondary particles and NPF events particular to this region (Gani et al., 2019; Kanawade et al., 2022; Laakso et al., 2006; Sebastian et al., 2022).

NPF is a crucial atmospheric process in which gas molecules, under favourable conditions, cluster to form new aerosol particles. These cluster exhibit sufficient stability to undergo subsequent growth through the condensation of additional gas-phase molecules, rather than reverting to the gas phase through evaporation. During an NPF event, a pronounced increase in nucleation-mode particles is observed, typically in the 3–5 nm diameter range (Aliaga et al., 2023; Kulmala et al., 2022; Zhang et al., 2026). As these nascent particles grow into the Aitken mode, their number concentration often increases further. This growth usually spans from about 1–10 nm up to 10–100 nm within a few hours, with growth rates typically ranging from a few to over 10 nanometer per hour. Typically, NPF events extend over synoptic spatial scales of hundreds of kilometres, persisting for a temporal duration of few hours facilitating the observation of changes in resultant particle populations. Within the realm of atmospheric science, NPF emerges as a pivotal process where gas-phase molecules converge to initiate the formation of solid or liquid particles. Different mechanisms have been proposed for these NPF events like binary water–sulphuric acid nucleation (Kulmala and Laaksonen, 1990; Seinfeld and Pandis, 2016), ternary water–sulphuric acid–ammonia nucleation (Cai et al., 2021; Kulmala et al., 2004), and ion-induced nucleation (Kirkby et al., 2016; Yu and Turco, 2001). In the overall aerosol loading, NPF contribution varies place to place and time to time but no doubt that it makes a significant part of that (Kerminen et al., 2018; Spracklen et al., 2010). To understand the role and contribution of NPF events properly we need to characterise them with getting their frequency, growth rate, and formation rate.

In this study, we investigate the temporal variability of size-resolved atmospheric ions and total particle concentrations at the IGP site and examine their relationships with concurrent meteorological parameters. From our observation data, we have also identified days on which NPF events occurred. We have applied different existing classification methods on the available data to identify NPF events and compare them. For these days, we have calculated typical NPF characteristic parameters (growth rate, formation rate and condensation sink). This analysis provides a comprehensive characterization of NPF and associated processes in a suburban environment of the Indo-Gangetic Plain.

2. Material and methods

2.1 Observation site:

We analyse the temporal variability of size-resolved ions and total particle concentrations using instrumental facilities established at the Atmospheric Observatory – Centre for Atmospheric Sciences (CAS-AO) (Rathore et al., 2025). The site is in Sonipat district, Haryana, India (28.99° N, 77.01° E; ~125 m a.s.l.). It is a suburban site, located ~65 km from the IIT Delhi main campus and ~10 km northwest of the northern boundary of Delhi (upwind). Agricultural land surrounds the site, while National Highways 44 and 34 intersect approximately 500 m from the sampling inlet. These highways represent the dominant nearby source of traffic-related emissions, in addition to advected regional sources. Some Industrial chimneys also exist on the other side of the cross highways. Residential areas lie approximately 300–400 m from the site which may be possible sources of diesel and household emissions. Small water bodies (ponds and fish farms) are present in the vicinity, and the Yamuna River flows within approximately 10 km of the site, potentially influencing local humidity and vapour precursors for particle formation and growth.

Figure 1 illustrates the measurement site's geographical context from Google Maps, including a zoomed-in view highlighting nearby roads and infrastructure (left), and a broader view showing its position within India (right). From a meteorological perspective, the CAS-AO acts as a receptor for air masses originating from upwind regions, including parts of the Middle East, Pakistan, and northern India. Its location, combined with proximity to major highways, agricultural activity, industrial sources, and residential areas, makes it well suited for investigating the interplay between local emissions, regional transport, and atmospheric processing of aerosols under subtropical conditions. The dataset used for the present paper is from May 2023 to Dec 2023.

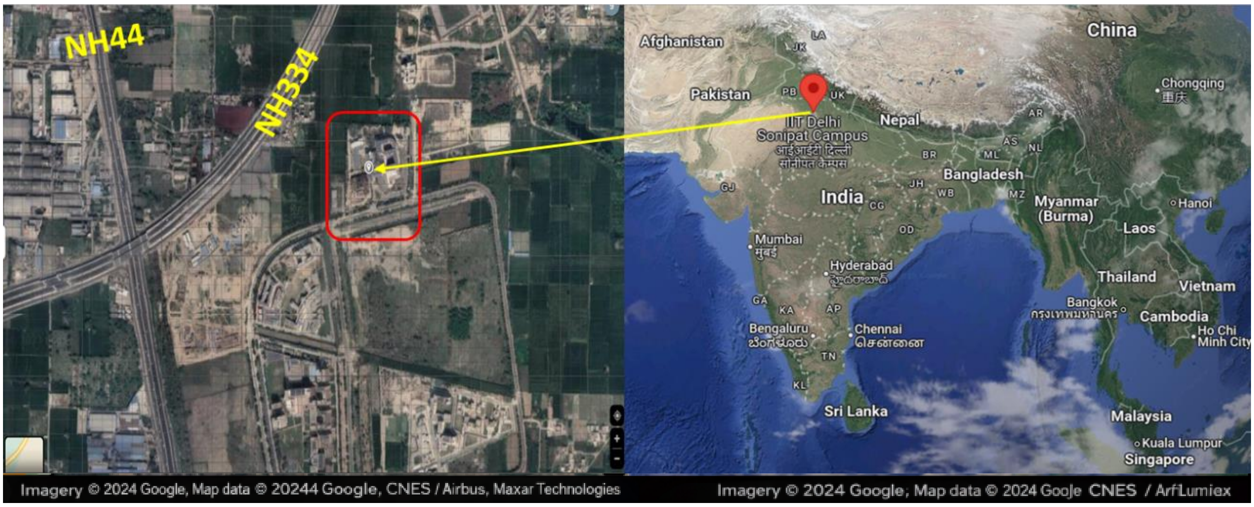

Figure 1: Map showing the location of the CAS-AO, including local surroundings (left) and its position within India (right). Base map from Google Maps (Maps data © 2024 Google, retrieved 15 January 2024).

2.2 Instrumentation

In this study, we use a Neutral Cluster and Air Ion Spectrometer (NAIS) and a Scanning Mobility Particle Sizer (SMPS). We operated the instruments on two independent sampling lines. We measure meteorological parameters using an Automatic Weather Station (AWS) installed on the rooftop of the same building (I-Tech Park building IIT Delhi's Sonipat campus). Unless otherwise specified, all diameters referenced in this study refer to mobility diameters. A brief Introduction of the instruments are as follows:

https://doi.org/10.5194/egusphere-2026-2212
Preprint. Discussion started: 15 June 2026

2.2.1 Neutral Cluster Air Ion Spectrometer (NAIS)

The Neutral Cluster and Air Ion Spectrometer (NAIS) measures size distributions of total particles (2–42 nm) and charged particles (0.8–42 nm), making it particularly suitable for studying atmospheric ions and particles (Mirme and Mirme, 2013). It employs parallel differential mobility analysis using two identical cylindrical DMAs, with one channel for positive ions and the other for negative ions together with a pre-conditioning unit that charges particles via unipolar ionization (corona discharge) before they enter the DMAs. This allows the instrument to resolve both naturally charged ions and neutral particles within its size range. Measurements of neutral clusters below ~2 nm carry significant uncertainty due to electrometer noise, corona-charging artefacts, and enhanced diffusional losses, particularly under high particle loadings during winter, which may affect absolute number concentrations (Kulmala et al., 2007, 2012). Above 2 nm size range, its sensitivity is constrained by the electrometers' detection limits and the corona charger, which restricts the smallest measurable concentrations and particle sizes (Manninen et al., 2011; Wagner et al., 2016). As such, we did not incorporate sub–2.5 nm total particle data in our analysis. NAIS offers several advantages: it measures both charged and neutral particles, provides high time resolution for capturing rapid changes in particle concentrations, and is relatively portable, enabling use in field campaigns. At the CAS-AO, the NAIS inlet consists of a 100 cm copper tube (3 cm diameter) mounted through a laboratory wall at ~5 m above ground level. Oriented downward without sharp bends, the downward inlet minimizes interference from raindrops. Unless stated separately, "total particles" or particles from NAIS refers to measurements encompassing both particles and ions.

2.2.2 Scanning Mobility Particle Sizer (SMPS)

We use the SMPS to measure particle size distributions at larger diameters (Aalto et al., 2001). The larger diameter particle concentration is used further to calculate condensation and coagulation sink. SMPS consists of an electrostatic classifier (TSI model 3080), a differential mobility analyser (DMA; TSI model 3081), an X-ray aerosol neutralizer (TSI model 3088), and a water-based condensation particle counter (CPC; TSI model 3785). The SMPS operates on the monotonic relationship between electrical mobility and particle size for singly charged particles. The neutralizer provides a stable charge distribution by bipolar charging. Then the classifier separate out particles of targeted diameter range (bins) by varying the voltage where monotonic relationship between electrical mobility and particle size of single-charge particles is used (Stolzenburg and McMurry, 2018; Tammet, 1995). The classified sample via differential mobility analyzer is further sent to CPC and the size distribution is determined (Kangasluoma et al., 2020; Stolzenburg and McMurry, 2018). Typical SMPS uncertainties arise from assumptions in the bipolar charge distribution (~5–10 % for particles in the 20–100 nm range), finite DMA transfer function width and inversion-related effects (resulting in a sizing uncertainty of ~5–10 %), flow rate calibration (±2–5 %), and CPC counting efficiency (>95 % above the lower detection limit, with reduced efficiency close to the cutoff diameter). The combined relative uncertainty in particle number size distributions is typically on the order of 10–20 % across the 12–570 nm size range, increasing toward the lower and upper size extremes (Johnson et al., 2020; Kangasluoma et al., 2020; Leppä et al., 2017).

2.2.3 Automatic Weather Station (AWS)

The AWS provides real-time measurements of meteorological parameters at 5-minute resolution (CIMO Guide No.8, WMO, 2017). Multiple instruments are clubbed together along with a digital logger. Measured parameters include air temperature, wind speed, wind direction, relative humidity, and solar radiation. Pair of instruments and weather parameters associated with them are: [Thermometer: Temperature; Anemometer: Wind Speed; Wind Vane: Wind direction; capacitive sensor: relative humidity; Barometer: atmospheric pressure; Pyranometer: radiation].

2.3 Methodology, conventions and data processing

In this study, the seasons are demarcated according to specific time frames. Winter spans December–February, spring March–April, summer May–June, monsoon July–September, and autumn October–November. These seasonal categorizations align with the framework outlined by the Indian National Science Academy (2018) (Gani et al., 2020). We divide the diurnal cycle into two time periods: day (6–18 h) and night (18–6 h). All temporal references throughout this study are expressed in local time (LT), specifically in Indian Standard Time (IST; GMT+05:30). This structured approach to seasonal and temporal divisions facilitates a more comprehensive understanding of the data and enables us to draw meaningful comparisons across different time frames. We have used the ions and total particles data from NAIS negative channel.

Data observed from AWS is presented in supplementary Fig. S1 which shows the typical seasonal diurnal variability of key meteorological parameters with significant variations in temperature (T), relative humidity (RH), wind speeds, and wind direction throughout the year. Winter (December–February) is characterized by low temperatures (~2–18°C), high relative humidity (~35–95 %), and low wind speeds (~1.5–4 m s^{-1}). During winter, the site frequently experiences shallow atmospheric boundary layers (depth < 100 m), particularly at night and in the morning. In contrast, the summer months (April to June) are marked by intense heat (T ~ 25 to 40 °C) and dry conditions (RH ~ 30–70 %). The monsoon season, spanning from July to mid-September, brings episodic heavy rainfall to the majority of the IGP. This period is characterized by slightly lower temperatures (T ~ 20 to 35 °C) compared to the summer. There may be some occurrence of relatively high temperatures, but mostly these are infrequent. Notably, the winds predominantly come from the northwest throughout most of the year, but during the summer and monsoon, they shift to south during the nighttime. The transitional seasons of spring (mid-February to March) and autumn (mid-September to November) bridge the meteorological extremes experienced in other seasons. Unfavourable meteorological conditions often exacerbate pollutant accumulation, leading to exceptionally high $PM_{2.5}$ concentrations (Guttikunda and Gurjar, 2012; Trivedi et al., 2014).

Researchers have proposed different classification frameworks in the literature to classify the observed particle size distribution (PSD) and identify the NPF events. Classification of PSD is essential because, it helps understand the frequency and characteristics of NPF events, with enabling quantification of particle formation and growth rates. However, the interpretation of NPF frequency is not solely a property of the atmospheric conditions but also depends on the choice of detection methodology, instrumentation sensitivity, and the specific classification logic applied.

https://doi.org/10.5194/egusphere-2026-2212
Preprint. Discussion started: 15 June 2026

One of the earliest systematic and widely adopted approaches for classifying NPF events was introduced by Dal Maso et al. (2005). This scheme is based on visual inspection of daily PSD and identifies an event when a distinct nucleation mode appears, persists for several hours (more than 1), and shows continuous growth toward larger diameters. Events are further categorized depending on whether growth and formation rates can be reliably quantified (Class Ia for standard very good visually appearance, Ib for days when event occur but visually not as well standard as Ia) or whether the event is less distinct events with weaker growth signatures (Class II). While days without such features are classified as non-events. This classification scheme involves visual interpretation and is therefore inherently subjective and time intensive. Still, it (sometimes in a modified form) remains a first-step diagnostic approach because it provides a structured and physically consistent way to separate event from non-event days in long-term aerosol datasets.

In the present study, we adopted the Dal Maso et al. (2005) classification framework with minor adjustments suited to our dataset. Distinguishing between subcategories Class Ia and Class Ib was not feasible, as most event-days exhibited an early and sharp burst of particles that obscured a clear separation between very strong and moderately strong events. Therefore, we grouped all clearly observable and well-developed growth events into Class I, while days showing NPF signatures under background influence or with less distinct growth were classified as Class II. Days without identifiable nucleation and growth were categorized as non-events. Days containing data gaps longer than 30-minutes were excluded. Days with even 30-minutes missing data during the critical daytime growth period were also discarded to avoid biased classification.

Another classification method Dada et al. (2018) detects initial cluster formation signals by searching periods with elevated 2–4 nm ion concentrations and investigates NPF signals using periods with elevated 7–25 nm particle concentrations. Based on daily particle size distributions, the method classifies days into four categories: Regional Events: Elevated period observed in 2–4 nm ions and subsequently in 7–25 nm particles (local formation with growth), Ion Bursts: 2–4 nm ions present but no elevated concentration observed in larger particles, transported events: 7–25 nm particles present without local ion formation (carried from elsewhere), and the Non-Events: Neither sufficient ion nor particle elevated concentration periods detected. This automated method identifies exact start, peak, and end times of events while excluding precipitation periods that interfere with ion measurements.

We apply this classification to observations from the CAS-AO in slightly modified way. Using the monthly mean particle number concentrations above 12 nm, we observed a substantial contribution from background aerosol loading and instrument noise, particularly during winter months, making it difficult to isolate the NPF growth signal in the full 7–25 nm range prescribed by Dada et al. (2018). Therefore, we restricted the particle growth criterion to the 7–12 nm range. This site-specific adaptation captures the transition from nucleation mode to Aitken mode while minimizing interference from pre-existing particles and instrument noise.

An alternative and recently developed technique for analysing NPF events is the nanoparticle ranking analysis method proposed by Aliaga et al. (2023). This approach offers a quantitative and objective framework to evaluate the likelihood and strength of NPF events by examining daily changes in particle number concentrations within the 2.5–5 nm size range ($\Delta N_{2.5-5}$). This parameter is calculated from smoothed time series by contrasting background (night-time) and active (daytime)

https://doi.org/10.5194/egusphere-2026-2212
Preprint. Discussion started: 15 June 2026

periods, yielding a single metric for each day that reflects the intensity of potential NPF. The days are then ranked according to this parameter and grouped into percentile classes or Gaussian modes of log($\Delta N_{2.5–5}$) which allows the probability and strength of NPF to be examined continuously rather than via a binary event/non-event classification. This method produces a continuous variable that facilitates the probabilistic assessment of both strong and weak NPF occurrences.

In this study, we applied the nanoparticle ranking analysis following the framework of Aliaga et al. (2023) to characterize NPF behaviour at CAS-AO. The ranking parameter was derived from the 3–5 nm particle number concentration (the lowest reliable size bin of our instrument), calculated as the difference between the daytime maximum concentration (6–18 h LT) and the nighttime median background concentration (21–6 h LT). This size range avoids contamination from the continuous molecular cluster mode at the lower end and reduces influence from primary anthropogenic emission sources, including traffic, at the upper end. A 2-hour rolling median smoothing was applied prior to the calculation to reduce short-term variability. The resulting $\Delta N_{3–5}$ values were ranked across the full observational period and grouped into 5 % percentile intervals.

Growth rate (GR) is defined as the temporal rate of change of particle diameter (dDp/dt), expressed in nm h^{-1}, representing the speed at which newly formed particles increase in size during growth events. In this study, GR was estimated using two independent approaches: maximum concentration method (using Gaussian function fitting) and appearance time method (using sigmoid function) (Kulmala et al., 2012). We have used particle number concentrations with size ranges (3–7 nm, and 7–20 nm). Particle number concentration has been smoothed using a rolling median filter to avoid noisy signals and temporary fluctuations. For the maximum concentration approach, the temporal evolution of each size bin concentration was fitted using a least-squares Gaussian function to determine the peak time. The growth rate was then calculated by performing a linear regression between peak times and corresponding particle diameters, expressed in nm h^{-1}. For the appearance method, the rising portion of each size-bin concentration curve was fitted with a sigmoid function to determine the 50 % appearance time (t_{50}). Growth rates were derived by regressing t_{50} values against particle diameter. The resulting growth rates distributions were visualized using box-and-strip plots to represent central tendency, spread, and event-to-event variability while preserving individual data points. Before fitting we have gone through the distribution evolution over time and find the window which represent the growth. We have gone through each fitting and peak specific diameter range (in the two category) where representative time was reliably detected.

The condensation sink (CS) was calculated from the aerosol particle number size distribution following the formulation described by Kulmala et al. (2012). The particle size distributions obtained by combining measurements from the NAIS for diameters below 40 nm and the SMPS for diameters above 40 nm, resulting in a continuous size spectrum spanning the nucleation and accumulation modes. The measured number size distribution expressed as $dN/dlogD_p$ was converted to particle number concentration in each size bin, and the contribution of each bin to the condensation sink was computed using the Fuchs–Sutugin correction factor to account for the transition regime between free molecular and continuum diffusion. The molecular diffusivity of sulfuric acid in air was calculated using temperature and pressure conditions representative of the measurement site (T = 293.15 K, P = 101325 Pa). The condensation sink was then obtained by summing the contributions from all particle size bins as CS = $4\pi D \sum \beta(Dp) Dp N(Dp)$, where D is the molecular diffusivity of sulfuric acid, $\beta(Dp)$ is the transition regime correction factor, Dp is the particle diameter, and $N(Dp)$ is the particle number concentration in each size bin. Data for the above 40 nm diameter range from SMPS were available for only a few days (mention in table T1). We have gone through days and further filtered days where NPF signals were less affected by other factors.

The particle formation rate (J) represents the rate at which new particles are formed at a given size and is expressed in cm^{-3} s^{-1}. In this study, the formation rate at 3 nm (J_3) was estimated following the formulation of Kulmala et al. (2012), given as Eq. (1) using the time evolution of particle number concentration in the 3–7 nm size range.

The formation rate was calculated as:

$$J_3 = \frac{dN_{3-7}}{dt} + CoagS \cdot N_{3-7} + \frac{GR}{\Delta D_p} \cdot N_{3-7} \tag{1}$$

where N_{3-7} is the particle number concentration in the 3–7 nm size range, $\frac{dN_{3-7}}{dt}$ is the temporal change in concentration, $CoagS$ is the coagulation sink representing losses due to coagulation with pre-existing particles, GR is the particle growth rate (nm h^{-1}), and ΔD_p is the width of the size interval (nm).

The first term represents the net increase in particle concentration, the second term accounts for losses due to coagulation, and the third term corrects for particles growing out of the size range. The coagulation sink was calculated using the particle size distribution following standard coagulation theory, considering interactions between newly formed particles and the background aerosol population. To reduce the influence of short-term fluctuations and measurement noise, the particle number concentrations were smoothed using a rolling median filter prior to derivative estimation. The formation rate was calculated only during identified NPF event periods where GR was reliably calculated and SMPS data was present to ensure physical relevance. For calculation of J_3, particle size ranges between 3–7 nm have been used and for J_7, we have utilised 7–12 nm as the 12–20 nm size range was influenced by other emission sources and instrument noise.

3. Results and discussion

3.1 Particle and ion number concentrations

Total particle and ion number concentrations at CAS-AO exhibit pronounced diurnal and seasonal variability (Fig. 2). Total particle concentrations in Fig. 2(a) shows clear daytime enhancements during May–June, while these features become more episodic and delayed during August–September. In contrast, October–December exhibits weak and poorly structured diurnal variability, with no clearly defined growth patterns.

During the warmer months (May–June), total particle concentrations show pronounced daytime enhancements. In August–September, these signatures remain visible but appear more episodic and slightly delayed compared to May–June. In contrast, the colder months (October–December) exhibit weaker and less structured diurnal variability, with no clearly defined growth patterns. In May–June, particle growth typically begins early in the day (around 6 h LT), while in August–September the onset appears somewhat delayed. These daytime enhancements are accompanied by a gradual shift toward larger diameters, indicating the growth of newly formed particles. At the smallest sizes, concentrations often appear as burst-like increases, followed by the onset of the characteristic banana-shaped growth pattern associated with NPF, which would be expected to extend further into larger diameters in corresponding SMPS observations.

Ion number concentrations in Fig 2(b) display broadly similar but generally more subdued features. Distinct midday enhancements are primarily observed during May and June, while distributions become progressively more uniform toward winter. Overall, the warmer months show clearer and more continuous growth signatures, indicating a strong seasonal modulation of NPF-related processes at the site. The smallest diameter ranges (below ~3 nm for total particles and ~2 nm for ions) are influenced by corona-generated charger ions and instrumental noise. Concentrations above 12 nm are dominated by pre-existing Aitken mode particles and background aerosol loading, making it difficult to isolate NPF signals at larger sizes. Horizontal dashed lines indicate the diameter ranges selected for subsequent analysis (3–12 nm for total particles and 2–4 nm for ions). These demarcated windows capture the size range where NPF signatures are most reliably observed and help refine the diameter thresholds used in standard NPF classification approaches.

Building on the size–time evolution shown in Fig. 2, the monthly statistical distributions of number concentrations within the selected diameter ranges are presented in Fig. 3. The figure shows total particles (7–12 nm and 3–5 nm) and ions (2–4 nm) as paired daytime and nighttime violin plots representing kernel density estimates. Within each violin, a box plot indicates the monthly median (central line), interquartile range (box), and 5–95 % percentiles (whiskers) for daytime (6–18 h LT) and nighttime (18–6 h LT) concentrations. Across the 7–12 nm size range in Fig. 3(a), particle concentrations show a seasonal and diurnal contrast. During summer (May–June), daytime median concentrations reach on the order of 3–5 × 10^3 cm^{-3}, approximately two to three times higher than nighttime levels (~1–2 × 10^3 cm^{-3}). The distributions are also substantially broader during the day, with upper percentiles extending well above 8 × 10^3 cm^{-3}, indicating episodic but intense production events rather than uniform background enhancement. In contrast, August and September exhibit more moderate daytime increases (median ~1–2 × 10^3 cm^{-3}) with reduced day–night contrast, while October–December show comparatively compact distributions and, in some cases (November–December), slightly higher nighttime medians, suggesting suppressed NPF and a stronger influence of background accumulation.

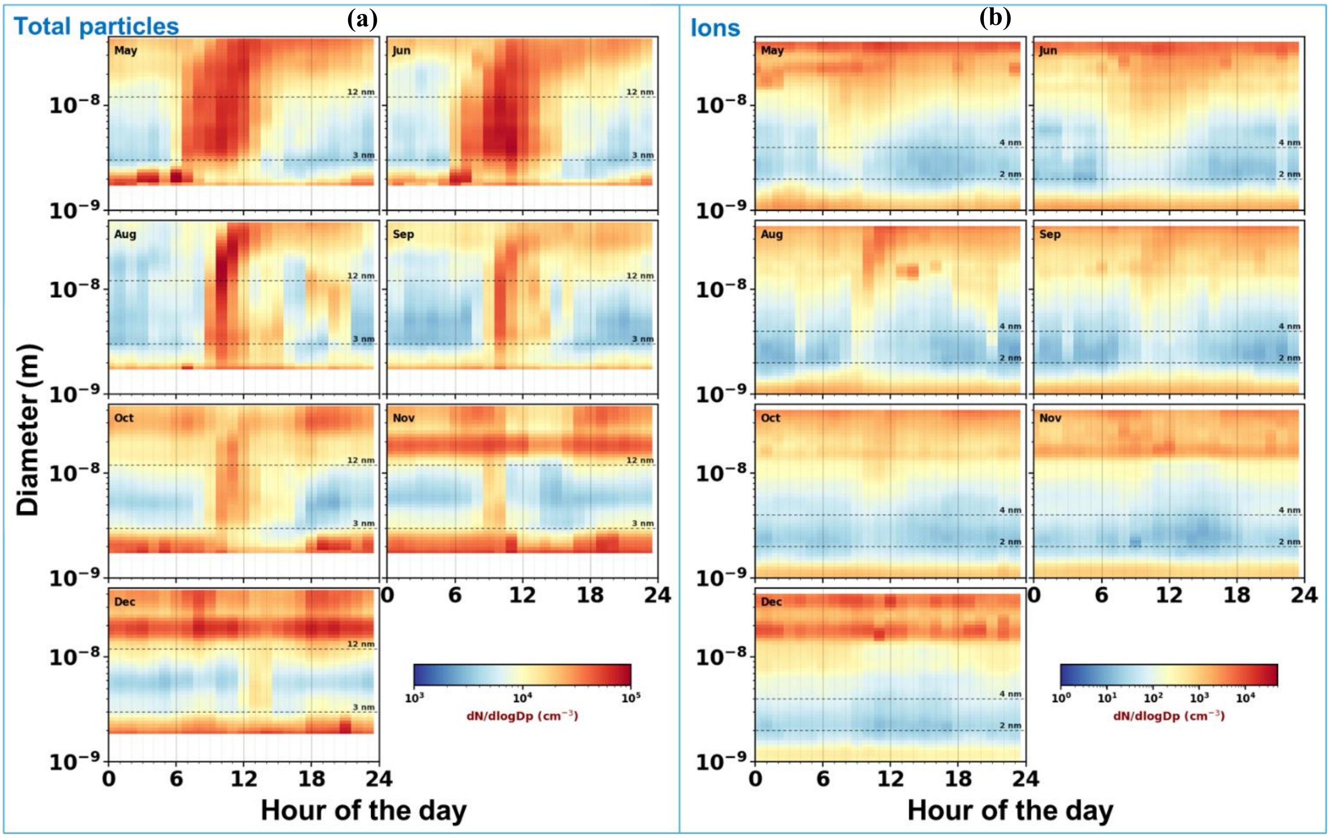

Figure 2: Heatmap showing size-resolved monthly mean variations of (a) total particles (ions + neutral) and (b) ions number concentrations for May, June, August, September, October, November, and December 2023 at CAS-AO. Horizontal dashed lines indicate the diameter bins used in further analysis (2 and 4 nm for ions; 3 and 12 nm for particles).

A similar pattern is observed for the 3–5 nm size range in Fig. 3(b), which represents freshly formed particles (relatively). In May and June, daytime medians approach ~3 × 10^3 cm^{-3} and exceed nighttime values by a factor of ~3–3.5, consistent with frequent and strong NPF activity. The enhancement weakens progressively toward late monsoon and post-monsoon months, with September and October showing only marginal day–night differences (~1.0–1.1 ratio). By November and December, nighttime concentrations become comparable to or slightly higher than daytime levels, reflecting the absence of sustained nucleation bursts and more stable aerosol conditions. In contrast, ion concentrations in the 2–4 nm range in Fig. 3(c) remain much lower in absolute magnitude (generally 5–12 cm^{-3}), with moderate daytime enhancement during May–August (day/night ratios ~1.5–2.5). However, unlike particles, ions display weaker seasonal variability and in late autumn–winter (October–December) occasionally exhibit higher nighttime medians, suggesting that ion abundance alone does not scale directly with the intensity of particle growth. Together, these distributional analyses quantitatively confirm the seasonal and diurnal patterns inferred from the heatmaps: strong and sustained daytime particle production during warmer months, a gradual weakening through the monsoon transition, and comparatively stable, background-dominated conditions in winter.

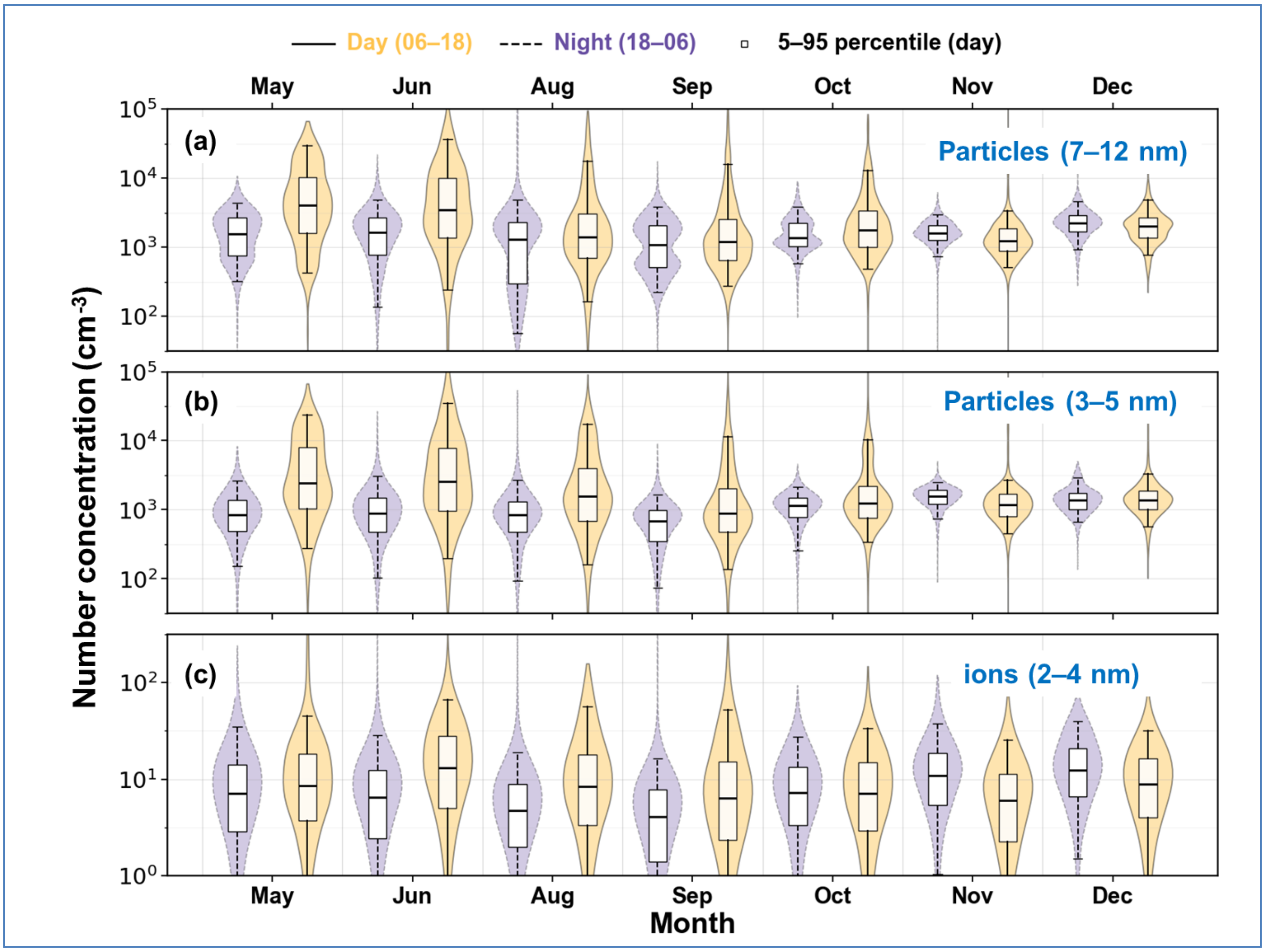

Figure 3: Monthly distributions of daytime (6–18 h LT) and nighttime (18–6 h LT) number concentrations, during May–December 2023, for (a) particles in the 7–12 nm size range, (b) particles in the 3–5 nm size range, and (c) ions in the 2–4 nm size range. Violin plots illustrate the full probability distribution of concentrations, while embedded box elements indicate the monthly median (central line), interquartile range (box), and 5–95 % percentiles (whiskers) of daytime (6–18 h LT) and nighttime (18–6 h LT) number concentrations. Daytime and nighttime periods are distinguished by solid and dashed outlines, respectively.

360

https://doi.org/10.5194/egusphere-2026-2212
Preprint. Discussion started: 15 June 2026

3.2 New particle formation at a suburban site upwind of Delhi

New particle formation (NPF) events were identified across the observational period (May–December 2023) at CAS-AO, Sonipat, representing a suburban site located approximately 50 km upwind of Delhi in the IGP (Rathore et al., 2025). The site experiences substantial seasonal variability in meteorological conditions and aerosol loading (Section 3.1), both of which modulate the frequency and intensity of NPF. Given that the IGP is characterised by elevated background aerosol concentrations and high condensation sinks, the detection and classification of NPF events is non-trivial and depends significantly on the choice of methodology. To address this, we applied three complementary classification frameworks of increasing complexity and objectivity, as described in the methodology section, and the results are presented below.

3.2.1 NPF event classification using different frameworks

Using Dal Maso et al. (2005) method, we identify a total of 10 Class I events (9% of total data days), 40 Class II (37 % of total data days) and rest 58 non-events days (54 % of total data days) over the 108-day study period. A seasonal modulation in NPF occurrence is evident. During May and June, the majority of days fall into Class I or Class II (11 out of 12 in May and 19 out of 23 in June), indicating frequent and well-developed particle formation. In contrast, the proportion of non-event days increases from September onward, with November and December dominated by non-event conditions. The framework proposed by Dal Maso et al. (2005), provides a physically intuitive and visually based separation of event and non-event days. It primarily relies on the size–time evolution of PSD and expert interpretation.

To complement this traditional visual classification and to reduce subjectivity, we further applied an automated event detection approach proposed by (Dada et al., 2018). This framework combines ion and particle number concentrations (7–25 nm size range for particles and 2–4 nm ion concentrations). This enables a more process-based distinction between local particle formation, transported event signatures, and ion burst events based on the concurrent behaviour of cluster-sized ions and larger particles. As detailed in methodology section, we restricted the elevated particle concentration criterion to 7–12 nm to account for site-specific noise characteristics. Using this methodology, warmer months (May–June) show the highest occurrence of regional NPF events (66 % and 86 % of total available days respectively). This indicates favourable conditions for local particle formation and growth. August, September and October have relatively fewer combined regional and transported event-days. Winter months (November, December) predominantly experience non-event days (88 % and 87 % respectively). Ion Bursts are relatively rare throughout the year, and we did not observe in our dataset.

Results are summarised in Fig. 4, which presents the monthly distribution of event categories from both classification schemes as stacked bar charts normalised to highlight seasonal contrasts. The stacked bar chart from this scheme demonstrates distinct seasonal patterns in NPF event occurrences. This seasonal transition may be attributed to favourable photochemical and dynamical conditions for nucleation during the warmer months. Winter conditions appear less conducive to sustained particle formation and growth. This can be possibly associated with reduced photochemical activity, effect of low wind speeds, usually high-pressure zone persistence and shallower boundary layer height typically observed during winter at this site.

Comparing the two schemes directly (Fig. 4), there is broad seasonal agreement: both identify May and June as the most active months and November–December as predominantly non-event. However, the Dada et al. (2018) classification consistently assigns a higher fraction of days to active categories than Dal Maso et al. (2005). For example, in August, Dal Maso identifies 50 % non-events whereas Dada assigns 60 % of days as regional or transported Events. This divergence is expected, as the Dada framework captures transported and partially developed events that the visual scheme places in Class II or non-event. The fraction of transported events (TE) is notably elevated in August–October, suggesting advection of particles or precursors rather than local formation during this transitional period.

Dada et al. (2018) can be regarded as an updated extension of the Dal Maso et al. (2005) classification, with consideration on lower size-range number concentrations and ion contribution to NPF events. This approach allows ion burst events and transported events to come into the picture. However, the distinction between regional and transported events is often subtle. The occurrence of transported Events suggests that particles formed in surrounding regions are being advected to the CAS-AO site. Usually, the days with high winds can efficiently transport the precursors as well as some fraction of particles. It is also possible that some transported Event classifications reflect anthropogenic emission signatures in the sub–12 nm size range rather than true NPF advection. Ion signals in the lower size range can be masked by external influences such as enhanced condensation sinks, local emissions, or meteorological conditions, which may obscure their detection by the instrument.

To make the classification picture clearer, we next applied the scheme proposed by Aliaga et al. (2023). Fig. 5 presents the median diurnal particle number size distributions for each 5 % percentile group using Aliaga et. al. (2023). The heatmaps span diameters from approximately 2–42 nm, enabling visualization of both nucleation-mode particles and their subsequent growth. Guiding horizontal lines at 3 and 5 nm are drawn to indicate the size range used for the ΔN ranking parameter. A systematic transition in NPF intensity is evident across the percentile ranks. The lowest percentile groups (0–40 %) show very weak or negligible formation activity, with relatively stable concentrations across sizes. Intermediate groups (40–65 %) begin to exhibit modest enhancement, suggesting partial or weak NPF activity. The highest percentile intervals (65–100 %) display clear burst and growth patterns initiating in the morning hours and extending toward larger diameters later in the day, indicative of sustained new particle formation and growth.

Fig. 6 presents a comprehensive analysis of NPF events using Aliaga et al. (2023)'s percentile ranking approach overlaid with event classification from Dada et al. (2018). NPF events identified by Dada et al. (2018) (regional and transported Events) cluster predominantly in the higher percentile groups (60–100 %), with very few events in percentiles below the 30th percentile. Within the high-percentile groups, May and June contribute the largest fraction of events, consistent with the seasonal patterns identified in both preceding classification schemes.

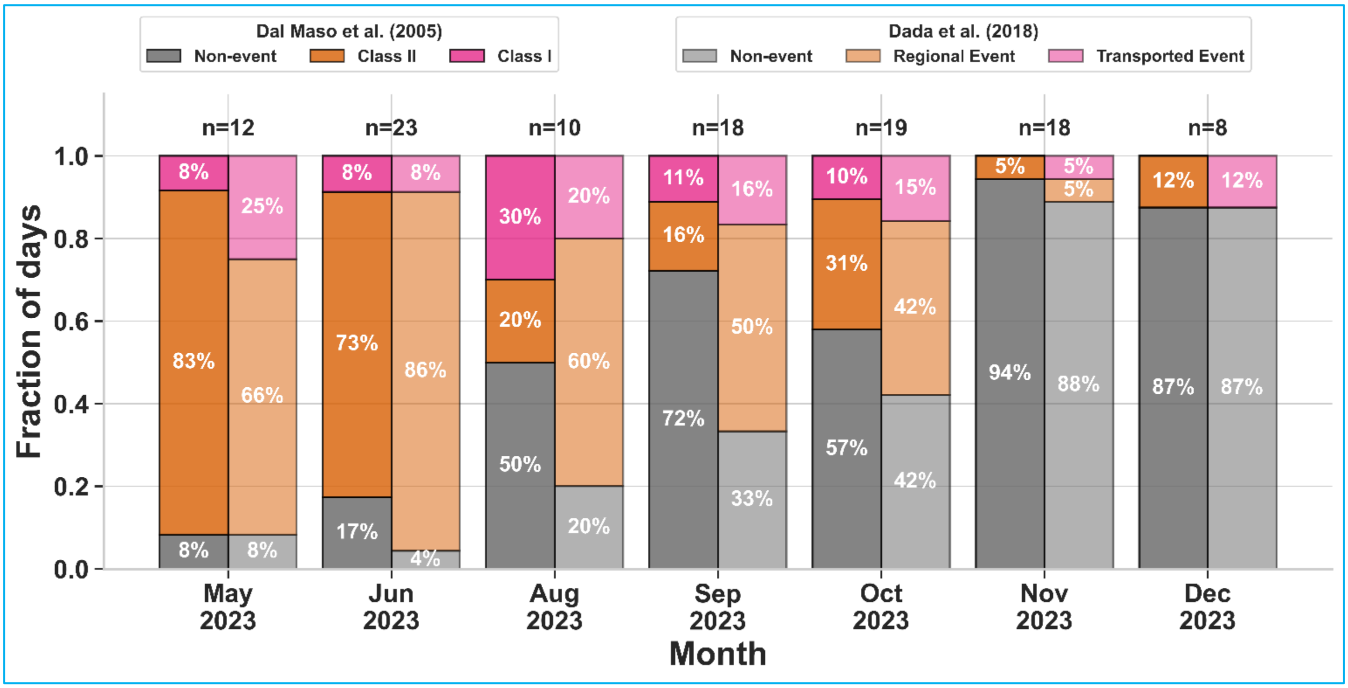

Figure 4: Monthly fraction of days at CAS-AO (May-December 2023) classified following the modified scheme of Dal Maso et al. (2005) left bars and Dada et al (2018) right bars. Days are categorized as Non-event, Class II, and Class I (for Dal Maso et al. 2005) and non-event, regional event, and transport event (for Dada et al. 2018). Numbers inside bars are percentage of days with total number of days in each category for each month, and at top of each bar "n" denotes the total number of days per month.

The combined application of the classification approach of Dada et al. (2018), rooted in the framework of Dal Maso et al. (2005), and the nanoparticle ranking analysis of Aliaga et al. (2023) offers complementary perspectives on NPF. The Dada et al. 2018 methodology focuses on the temporal evolution of ion and particle size distributions within individual days, categorizing events according to their developmental characteristics (e.g. regional formation, transported influence, or weaker ion-related activity), and thereby emphasizes process-level interpretation based on daily growth signatures. In contrast, the Aliaga et al. (2023) ranking method evaluates NPF intensity using a statistical metric derived from longer-term variability in a selected size range (3–5 nm in this study) placing each day within a broader context of event strength over the full data set. When applied together, the two approaches show general consistency. Days categorized as clear formation events in the Dada et al. (2018) framework tend to fall within the higher ΔN percentiles in the ranking analysis. At the same time, the agreement is not exact for some days, which is expected given the different conceptual bases of the methods. The Dada classification may identify transported bursts based on their temporal development, whereas the percentile-based approach quantifies the magnitude of concentration enhancement without explicitly distinguishing its physical origin. In both cases, possibly local anthropogenic sources, particularly traffic emissions given the site's suburban location upwind of Delhi, may influence the elevated particle concentrations whether from regional NPF, transported growth, and so the classification outcome. Therefore, neither framework alone can fully resolve the underlying mechanisms without additional supporting analyses.

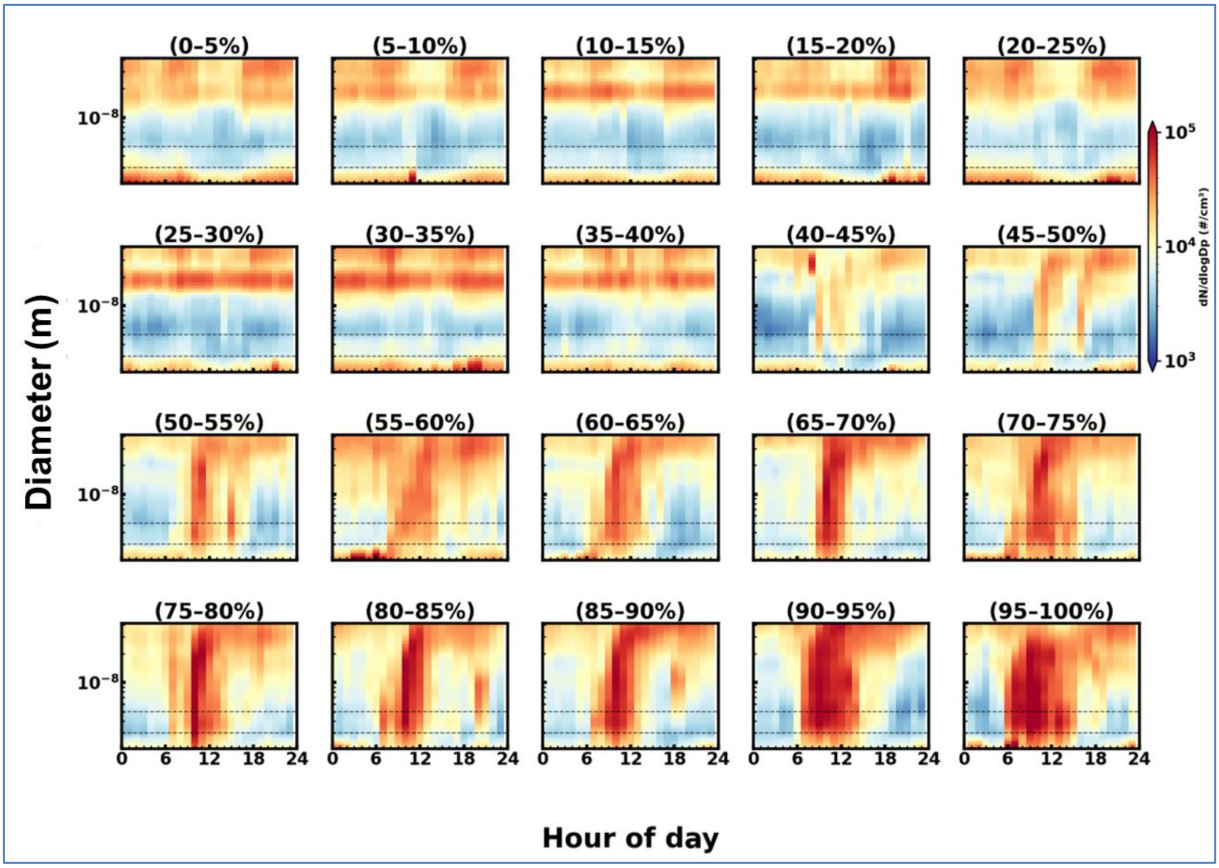

Figure 5: Daily median particle number size distributions grouped in 5 % intervals based on $\Delta N_{2.5-5}$ ranks. Each panel shows the diurnal evolution of particle size distributions for a specific percentile interval., with colour indicating particle number concentration (cm^{-3}). Horizontal guiding lines are drawn at 3 nm and 5 nm to help in visualizing the ranking parameter.

Each of the three classification frameworks carries inherent limitations that are particularly relevant in the suburban context of CAS-AO. The Dal Maso et al. (2005) method, despite its physical intuition, depends on manual visual inspection, introducing observer subjectivity and limiting reproducibility; the high fraction of Class II events in this dataset (37 %) reflects the difficulty of unambiguously resolving nucleation modes against the elevated background aerosol typical of an environment downwind of a megacity. The Dada et al. (2018) method reduces this subjectivity through automation, but its reliance on 2–4 nm ion signals make it vulnerable to masking by the high condensation sinks and anthropogenic aerosol loading characteristic of this site. The Aliaga et al. (2023) ranking approach avoids categorical ambiguity by assigning a continuous intensity metric to every day, but ΔN_{3-5} is not source-specific: elevated sub–5 nm concentrations can arise from traffic emissions or other primary sources rather than NPF, a concern that is amplified at a site located upwind of Delhi where anthropogenic precursor and primary particle loads are substantial. All three methods are additionally sensitive to the pre-existing aerosol loading, a high condensation sink suppresses the observable nucleation signal regardless of the actual nucleation rate, meaning that genuine NPF events may be systematically underestimated or misclassified under the polluted conditions frequently encountered at this site. These limitations reinforce that the three methods should be treated as complementary rather than independently sufficient diagnostics, and that confident mechanistic attribution requires supporting data on precursor gas concentrations, air mass origin, and boundary layer dynamics.

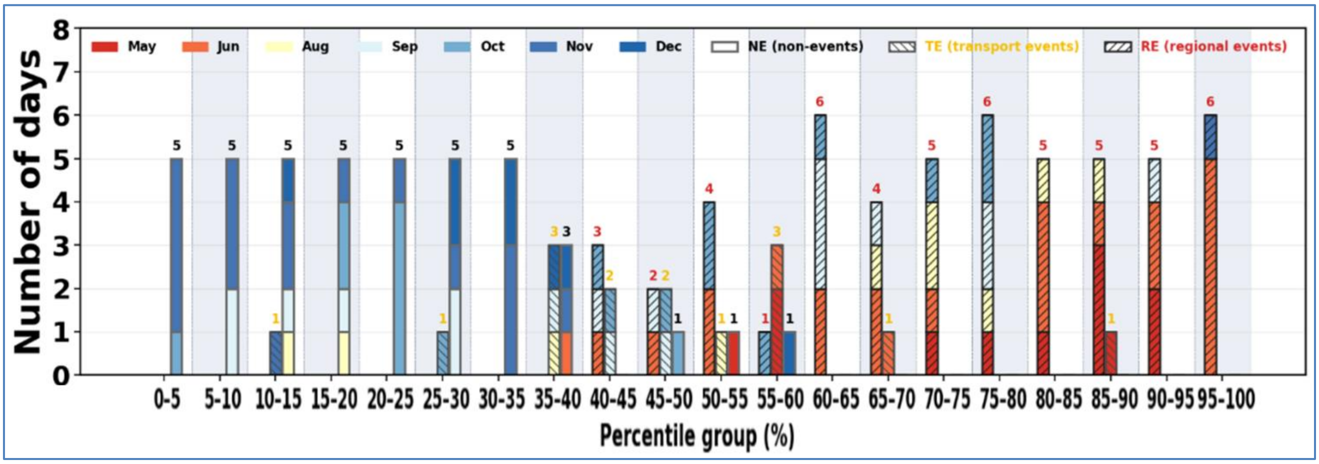

Figure 6: Seasonal distribution of Dada et al. (2018) event categories, grouped by $\Delta N_{2.5-5}$ percentile intervals. The x-axis displays percentile groups based on ΔN_{3-5} particle concentration rankings (from 0–5 % to 90–95 %), while the y-axis shows the number of events. Each bar is color-coded by month and differentiated by pattern for regional events (forward hatched), transported events (backwards hatched) and non-events (solid). Total event-days observed in the analysis period for each percentile are marked at top of the bars.

https://doi.org/10.5194/egusphere-2026-2212
Preprint. Discussion started: 15 June 2026

3.2.2 NPF parameters: growth rates, condensation sink and formation rates

Figure 7 presents the distribution of particle growth rates (GR) for size ranges (3–7 nm and 7–20 nm), derived using the maximum concentration method (using Gaussian fitting) and appearance time methods (using sigmoidal fitting). The distributions are shown as boxplots representing the median and interquartile range (IQR). Both methods exhibit broadly consistent distributions within each size range, with overlapping IQRs and similar median values. Across all events, median growth rates for the 3–7 nm range are 10.6 (7.9–15.9) nm h^{-1} (appearance time) and 14.7 (10.2–18.0) nm h^{-1} (maximum concentration), while for the 7–20 nm range they increase to 16.8 (13.9–26.6) nm h^{-1} and 19.0 (16.4–20.4) nm h^{-1}, respectively. This systematic increase in GR with particle size is evident across both methods and may possibly suggest enhanced condensational growth at larger diameters. Substantial event-to-event variability is observed, particularly in the 3–7 nm range. In contrast, the 7–20 nm range exhibits higher central values and relatively narrower dispersion for the max conc. method. This indicates that early-stage growth is more sensitive to variable atmospheric conditions, whereas growth at larger sizes is comparatively more stable.

Figure 8 presents a global comparison of particle GR in the 3–7 nm and 7–20 nm size ranges across diverse atmospheric environments, including remote, high-altitude/background, marine/coastal, rural, polluted regional, and urban locations. Literature-reported median GR values are compiled from long-term and multi-site analyses e.g., (Iida et al., 2008; Manninen et al., 2010; Yli-Juuti et al., 2011; Herrmann et al., 2014; Kontkanen et al., 2016; Kulmala et al., 2017; Kerminen et al., 2018; Sellegri et al., 2019; Yu et al., 2020; Stolzenburg et al., 2023; Lampilahti et al., 2025) and are shown as circles with horizontal whiskers indicating the reported variability range (min–max where available). The values from the present study conducted in the IGP, Sonipat CAS-AO, derived using max conc. and appearance time methods, are highlighted with star symbols. For consistency, entries with closely matching upper bounds (e.g., 7–15 nm or 7–25 nm) are included in the 7–20 nm panel for comparative purposes. In the 3–7 nm size range, the GR values from the present study fall within the upper range of urban and polluted regional environments, exceeding most background and remote site values. In the 7–20 nm range, the max conc. derived values remain closer to the central tendency of urban literature reports, whereas the appearance time method highlights episodes of enhanced growth that shift the site toward the upper envelope of reported values. The comparison suggests that the particle growth in the IGP is elevated compared to cleaner environments, particularly at larger particle sizes consistent with elevated condensable vapour concentrations expected in the anthropogenically influenced IGP boundary layer.

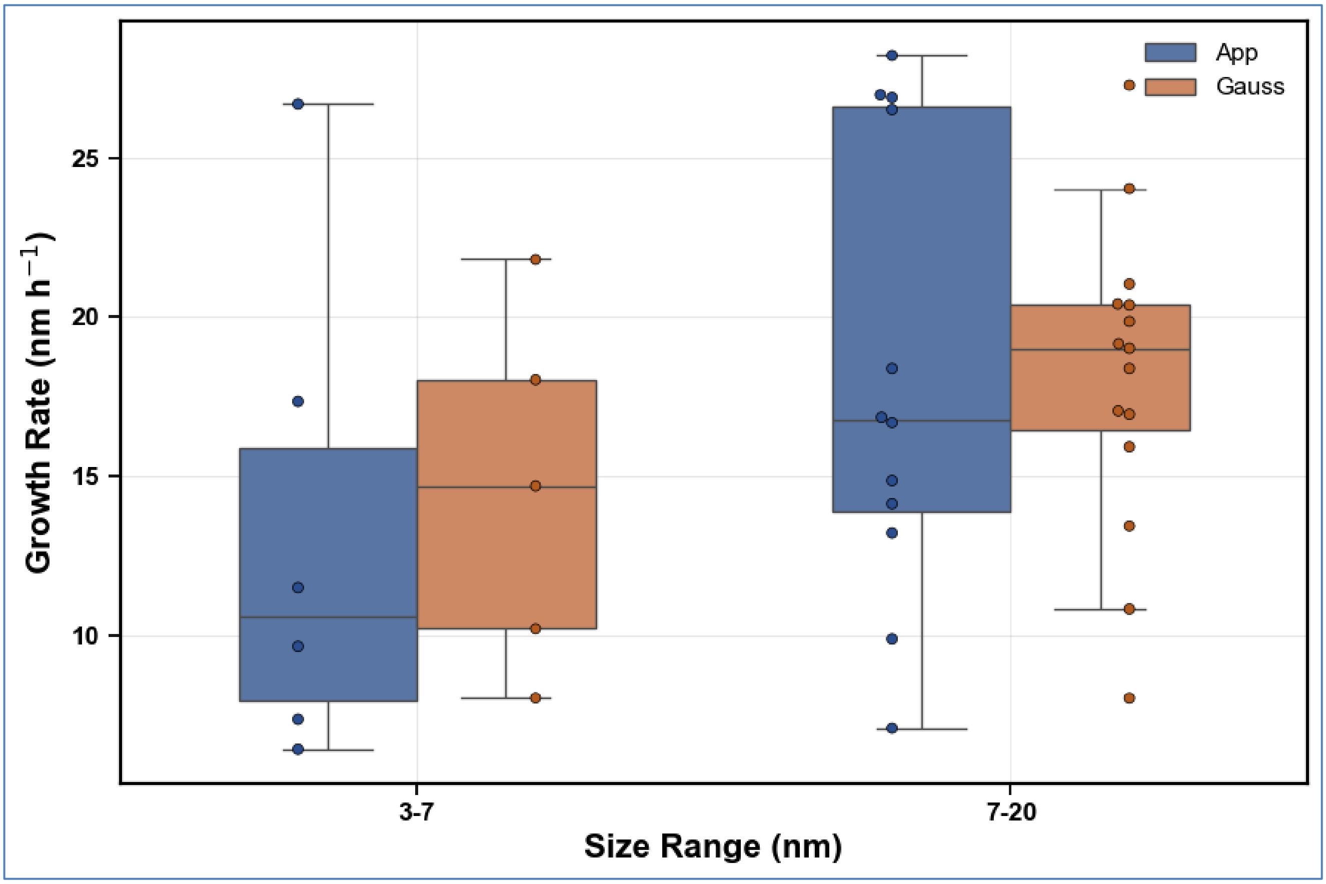

Figure 7: Distribution of particle growth rates (GR) in size ranges 3–7 and 7–20 nm derived using the Maximum concentration method (using Gaussian fitting) and appearance time methods (using sigmoid function). Boxplots show the median and interquartile range, with whiskers representing the range excluding outliers. Individual markers denote event-wise GR values.

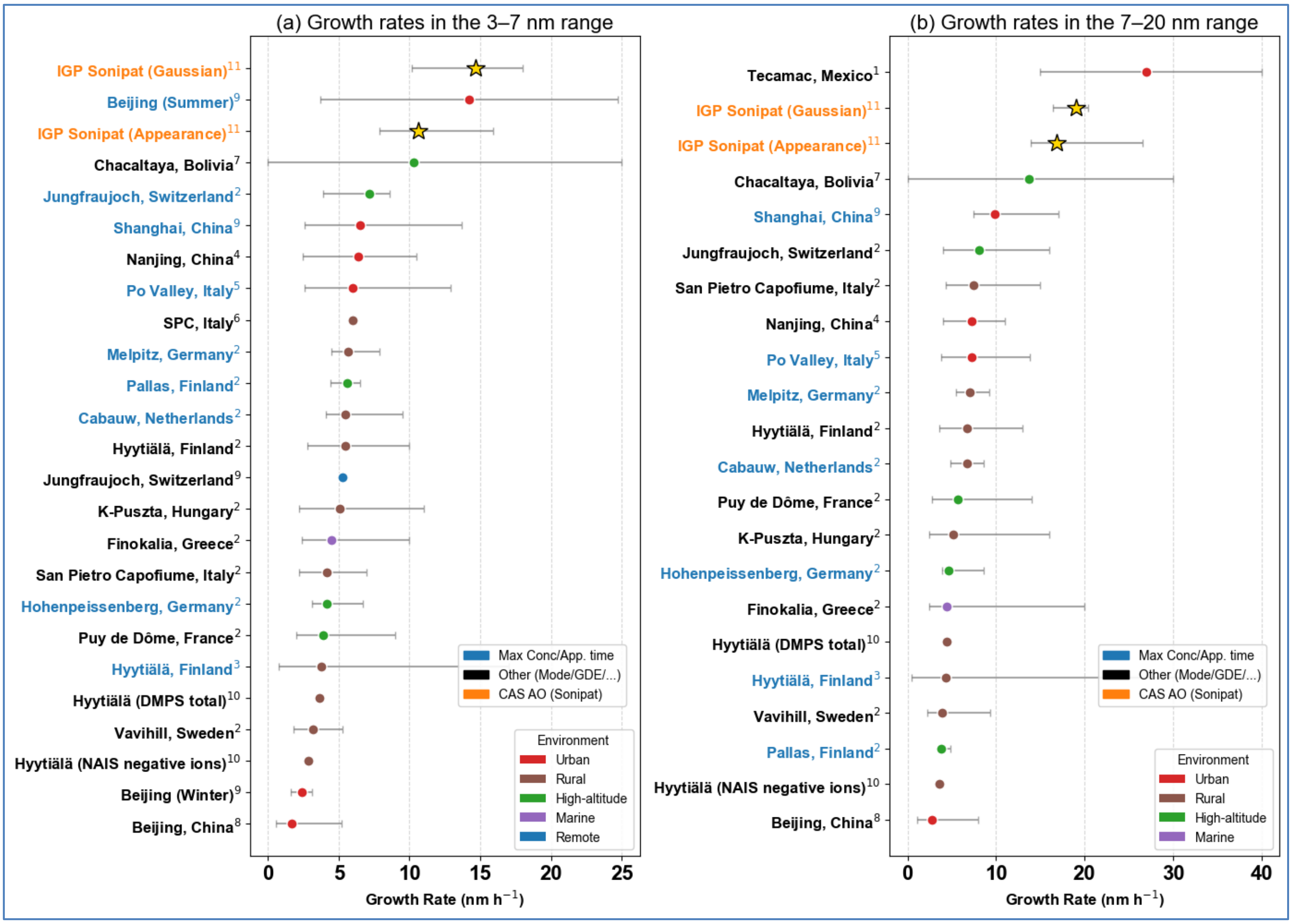

Figure 8: Global comparison of particle growth rates (GR) in the (a) 3–7 nm and (b) 7–20 nm size ranges across diverse atmospheric environments. Circles represent reported median GR values from literature studies, with horizontal whiskers indicating the reported variability range (min–max where available). Colours denote environment type (high-altitude/background, marine/coastal, rural, and urban). Star symbols highlight values from the present study conducted in the (CAS-AO) Indo-Gangetic Plain (IGP), Sonipat, derived using Gaussian peak fitting and appearance time methods. Growth rates are expressed in nm h^{-1}. Entries with slightly different upper size bounds (e.g., 7–15 nm or 7–25 nm) are included in the 7–20 nm panel for comparison and are noted in the corresponding references. (1: Iida 2008; 2: Manninen 2010; 3: Yli-Juuti 2011; 4: Herrmann et al., 2014; 5: Kontkanen 2016; 6: Kulmala 2017; 7: Sellegri 2019; 8: Yu 2020; 9: Stolzenburg et al., 2023; 10: Lampilahti 2025; 11: This Study).

Figure 9 (a) presents the composite diurnal behaviour of particle number size distributions and (b) condensation sink for event and non-event days. The left panels show the median particle number size distributions as a function of time of day for event and non-event days, derived from the combined NAIS–SMPS measurements. It may be noted that the heatmap shows corona charger ions below 3 nm diameter range and above 20 nm size range NAIS data is probably influenced by multiple charged particles. Event-days exhibit a clear daytime nucleation mode followed by particle growth. In contrast, non-event days show relatively stronger accumulation-mode particles and weaker nucleation-mode signatures. The right panel shows the diurnal variation of the median condensation sink values, where event-days consistently exhibit lower CS values compared to non-event days, particularly during the daytime nucleation window. The shaded region highlights the typical time period when nucleation and particle growth are observed. The median CS on event-days was (median: 0.024 s^{-1}, IQR: 0.016–0.033 s^{-1}) approximately half that on non-event days (median: 0.046 s^{-1}, IQR: 0.034–0.062 s^{-1}). This difference is statistically significant (Mann–Whitney U test, $p < 10^{-17}$) with a large effect size (rank-biserial = 0.71), indicating a strong separation between event and non-event conditions.

During the typical nucleation window (~6–18 h LT), event-days consistently maintain lower CS values, particularly during late morning to early afternoon, when particle formation and growth are most active. The reduced CS during these periods implies a weaker scavenging environment, allowing newly formed clusters to grow to detectable sizes. Typical day time CS values observed in Delhi has been reported more than ~0.06 s^{-1} to sustain NPF events (Ali et al., 2025). Studies in Beijing have also found that NPF events typically occur when CS remains below ~0.03 s^{-1}, while higher values suppress cluster survival (Deng et al., 2021). In contrast, much lower condensation sinks (~10^{-3}–10^{-2} s^{-1}) are typical of cleaner environments such as the boreal forest site in Helsinki, highlighting the strong influence of background aerosol loading on NPF occurrence across different atmospheric regimes. The event-day CS observed here (median 0.024 s^{-1}) falls between the suppression thresholds reported for Delhi and Beijing, suggesting that NPF at this site operates near the upper boundary of conditions permissive for cluster survival in polluted environments.

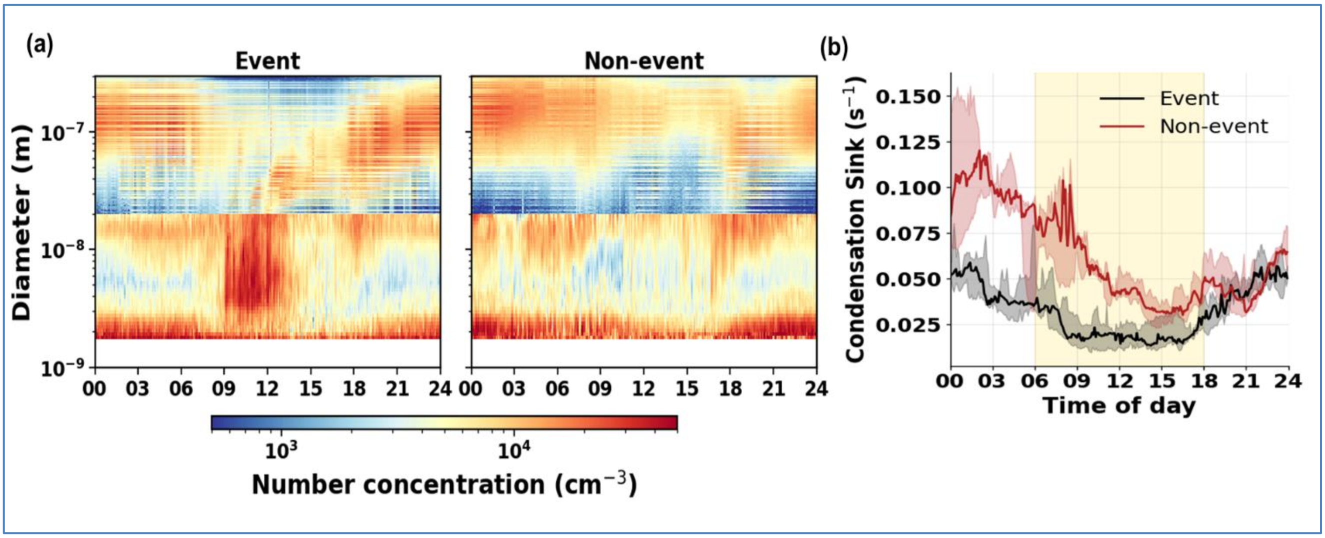

Figure 9: (a) Diurnal composite aerosol particle size distributions and (b) condensation sink during new particle formation (NPF) event and non-event days. Left panel (a) shows the median particle number size distribution as a function of time of day for event-days (left) and non-event days (right), combining NAIS (sub–20 nm) and SMPS (>20 nm) measurements. The colour scale represents particle number concentration (cm^{-3}), and the y-axis is shown in logarithmic diameter scale. The right panel (b) shows the diurnal variation of the condensation sink (CS) for event-days (black) and non-event days (red), with shaded regions indicating the interquartile range (25–75 %). The shaded vertical band highlights the typical nucleation time window (6–18 h LT).

Studying NPF in polluted environments presents substantially greater challenges compared to relatively clean conditions. In our measurements, several days exhibited visually identifiable NPF-like signatures; however, these were frequently obscured by irregular and non-systematic contributions from multiple emission sources. These sources introduced additional modes in the particle number size distribution, often overlapping with or masking the growing nucleation mode. In some cases, the pollution-related modes dominated the signal, completely suppressing the visibility of NPF, whereas in other cases, the growth appeared only as a shoulder adjacent to a broader pollution plume. In such environments, traditional manual approaches relying on visual inspection become less reliable, and fully automated methods often fail to capture the complexity of the data.

Further complications arise from instrumental noise and meteorological variability. Wind fluctuations and precipitation intermittently dilute or distort the particle concentrations, leading to fragmented or discontinuous signatures. While rainfall is less frequent during summer and winter, elevated wind speeds during these periods can still significantly perturb the observed distributions. Together, these factors introduce substantial variability that complicates the identification and interpretation of NPF events.

The classification of NPF events under such conditions inherently carries uncertainity. The widely used visual framework like Dal Maso et al. (2005) classification scheme relies on visual interpretation and investigator judgment. Variations in color scale, plotting choices, and subjective interpretation can lead to inconsistencies. While such discrepancies are minimal in cleaner environments, polluted conditions introduce substantial ambiguity, resulting in lower inter- and intra-observer agreement.

Semi-automated and automated approaches, such as those proposed by Dada et al. (2018) method and Aliaga et al. (2023) method, offer promising alternatives. However, these methods typically rely on detectable enhancements in particle number concentrations within specific size ranges. In polluted environments, such enhancements are often masked, fragmented, or confounded by overlapping sources, limiting the effectiveness of these techniques. Consequently, careful day-by-day inspection remains necessary to identify genuine NPF signals.

Despite these methodological challenges, consistent patterns emerge from the combined classification and concentration analyses, providing insight into the underlying processes governing NPF at this site. All the methods agree on the fact that the summer is more conducive to the NPF events whereas winter periods are generally less favorable for sustained particle formation. This seasonal variability is apparent in particle number concentration but ion concentrations does not show much variability across year. This may be interpreted as ion availability is not the primary constraint on particle formation in this region. This observed decoupling between ion and nucleation-mode particle dynamics signals towards the fact that controlling influence of precursor vapor abundance and the condensation sink are play a more important role in controlling particle survival and growth. This interpretation is further backed up with the event distribution: the prevalence of sufficient transported events alongside the absence of Ion Bursts**.** Instances of particle growth occurring in the absence of local ion enhancement provide evidence for the prioritising of neutral cluster pathways or the advection of particles nucleated upwind. So in the high-condensation-sink environment of the IGP, ion-induced pathways are likely secondary to neutral mechanisms in driving regional aerosol populations. Further chemical characterization of precursor vapours would be required to confirm these pathways.

The estimation of particle GR is similarly affected. Most existing studies e.g., (Kulmala et al., 2012; Lehtipalo et al., 2014; Paasonen et al., 2018) focus on relatively clean conditions characterized by distinct lognormal modes. In contrast, our dataset frequently exhibits multiple overlapping modes with varying intensities, requiring manual intervention in the fitting process. Due to these non-ideal conditions, it is not always possible to estimate GR over a consistent size range across all days. In several cases, the growing mode is only weakly visible or appears as a shoulder of a dominant pollution-related mode.

The two typical representative days which are influenced by the pollution source spike are shown in Fig. 10. In Fig. 10 (a) for 17 August 2023, the particle number increased due to NPF event is much stronger than any pollution spikes in the data and the growth rate was possible to calculate. But in Fig. 10 (b) for 15 October 2023, particle size distribution, it is evident that there is nucleation and some growth signatures. Still wind and pollution spikes distort the size distribution and it is not possible to reliably obtain a growth rate. Fragmented and ambiguous features presented in the data make the estimation unreliable and more uncertain. Despite these limitations, formation rates were calculated where feasible. Also it is to be noted that only 11 NPF days where overlapping SMPS and NAIS measurement days were available in which after filtering only 3 such days were possible where we could reliably calculate the growth rate. Parameters for each days are presented in the Table 1. We have estimated that the formation rate value range between 50–60 $cm^{-3}s^{-1}$ for J_7, where the number distribution is used between 7–12 nm range.

https://doi.org/10.5194/egusphere-2026-2212
Preprint. Discussion started: 15 June 2026

The measurement period included episodic pollution plumes with particle number concentrations occasionally rise abruptly or sometimes produced concentration enhancements comparable in magnitude and timing to NPF growth signals. Wind-driven variability further introduced choppiness in size-bin time series. Growth rates reported here were derived after careful manual screening to minimise such contamination and individual days heatmaps are presented in supplementary Fig. S5. However, residual influence cannot be entirely excluded. Robustly separating NPF mode enhancement from superimposed pollution signals remains a methodological challenge that warrants dedicated attention in future work, particularly for suburban and urban sites where both sources co-exist.

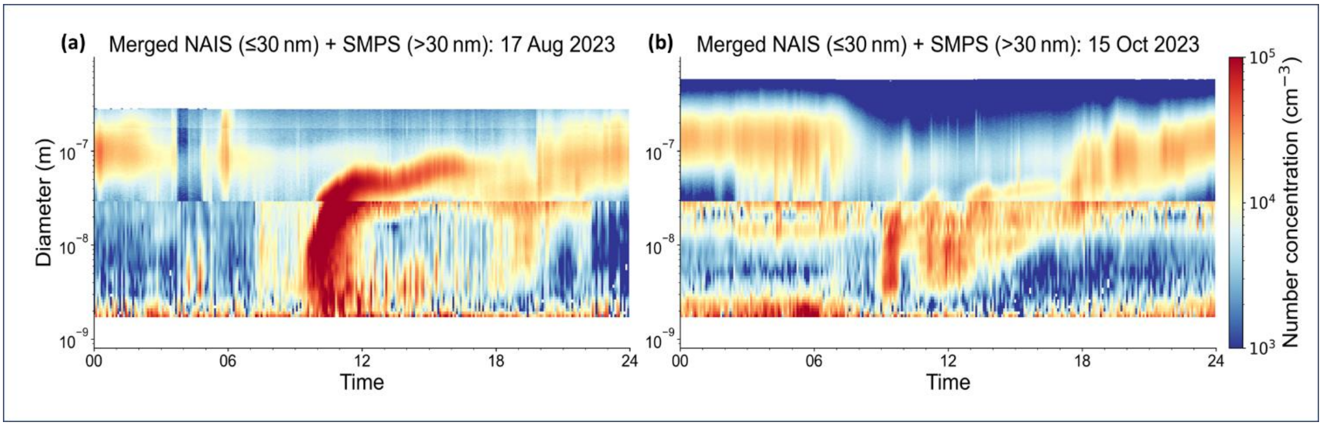

Figure 10: Time–diameter evolution of particle number size distributions for selected days (17 August 2023 (a) and 15 October 2023 (b)) at CAS-AO, obtained from merged NAIS (≤ 30 nm) and SMPS (> 30 nm) measurements. The colour scale represents particle number concentration (cm^{-3}) on a logarithmic scale.

Table 1: Particle formation rates at 3 nm (J_3) and 7 nm (J_7), growth rates, and condensation sink for NPF days at CAS-AO. Growth rates (GR_{3-7} and GR_{7-20}) are derived for the 3–7 nm and 7–20 nm size ranges, respectively. For the J_7 the growth rate has been calculated for the sub size range between 7 and 20 nm accordingly where it was reliably possible to calculate it. For the J_7, particle number concentration between 7 to 12 nm is used to avoid instrument artifact and possible other emission sources.

	($cm^{-3}s^{-1}$)	($cm^{-3}s^{-1}$)	(nmh^{-1})	(nmh^{-1})	(s^{-1})
17-08-2023	-	50.0	-	27.3	0.029
18-08-2023	80.8	53.5	26.7	19.0	0.026
07-10-2023	-	59.2	-	15.9	0.018

https://doi.org/10.5194/egusphere-2026-2212
Preprint. Discussion started: 15 June 2026

3.3 Role of condensation sink and meteorological conditions on NPF occurrence:

During the post-monsoon and winter transition period over the Indo-Gangetic Plain, aerosol loadings are typically elevated and dominated by accumulation-mode particles, leading to enhanced condensation and coagulation sinks. Consequently, clear and sustained NPF events are generally less frequent during this season which has been demonstrated by the classification results in section 3.2. Nevertheless, intermittent NPF events are occasionally observed under favourable combinations of reduced sink strength and supportive meteorological conditions. To illustrate the processes enabling NPF under such otherwise unfavourable background conditions, we examine in detail the period from 5–10 October 2023, which includes a well-defined NPF event on 7 October 2023.

Figure 11 illustrates the time-diameter evolution of particle number concentrations and sink parameters during 5–10 October 2023, encompassing both NPF and non-event days. The figure combines size-resolved measurements from SMPS in Fig. 11 (a), the NAIS negative-ion channel in Fig. 11 (b), and the corresponding condensation sinks in Fig. 11 (c). The SMPS and NAIS spectrograms illustrate the temporal evolution of particle populations across the nucleation, Aitken, and accumulation modes. Dashed horizontal lines mark reference diameters at 2 and 25 nm. All panels share a common time axis, enabling direct comparison between particle size distributions and sink dynamics over the same period.

Figure 12 summarizes the synoptic and local meteorological conditions during the same period encompassing the NPF event on 7 October 2023. In Fig. 12 (a), the Wind speeds exhibit moderate variability throughout the period, with the event-day characterized by predominantly north-westerly flow and moderate wind speeds, conditions associated with enhanced ventilation and lower background aerosol accumulation. Wind direction shows intermittent variability on non-event days, suggesting changing air mass influences that may contribute to fluctuating aerosol loadings. Concurrent in Fig. 12 (b), low relative humidity (~35 %) and elevated temperature (~30 °C) on 7 October 2023 further support favourable nucleation conditions. In Fig 12 (c) shows the global, diffused and direct solar radiation which has not very significant changes. Similar meteorological features may also occur on non-event days; however, NPF occurrence reflects the combined influence of favourable meteorology, precursor availability, and sufficiently reduced sink conditions, no single factor being independently sufficient.

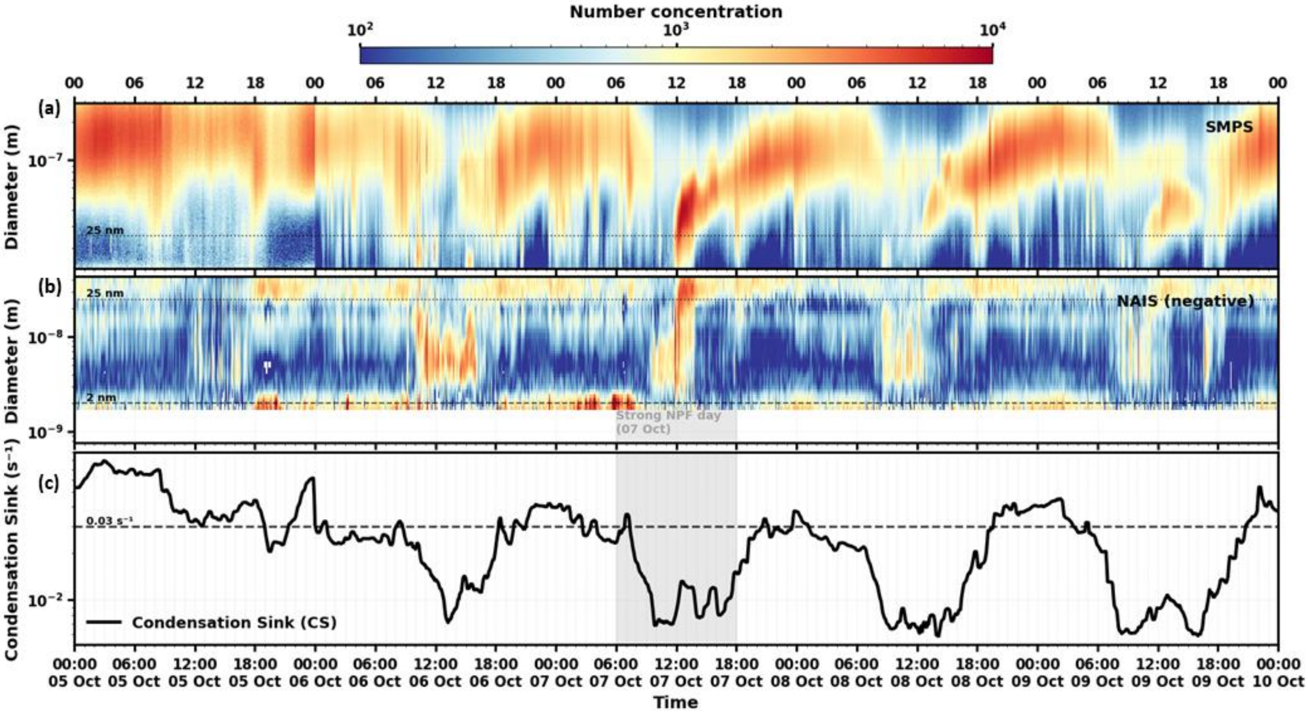

Figure 11: Time–diameter spectrograms of particle number concentration measured by (a) SMPS (top) and (b) NAIS negative channel (middle) from 5–10 October 2023, together with the (c) condensation sink (CS) (bottom). Colour indicates number concentration (cm^{-3}) on a logarithmic scale. Horizontal dashed lines mark 2 nm and 25 nm particle diameters. The shaded region highlights the new particle formation (NPF) day (07 Oct). The bottom panel shows CS (black) with the dashed line indicating the CS = 0.03 s^{-1} threshold. All panels share a common time axis.

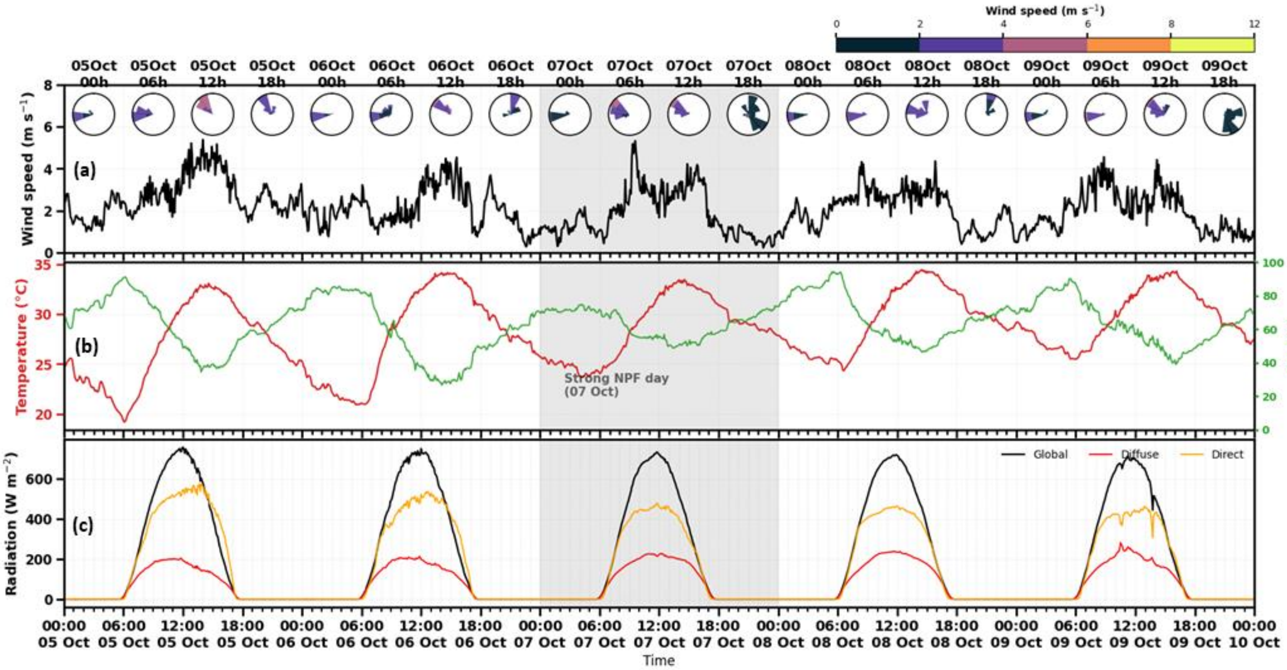

Figure 12: Meteorological conditions during the NPF observation period (5–10 October 2023). Time series of (a) wind speed as wind roses for each 6 hours and wind direction, (b) air temperature and relative humidity (RH), and (c) global, diffuse, and direct solar radiation measured at the CAS-AO. The shaded region highlights the NPF event-day (7 October 2023). All variables are shown at their native temporal resolution, with a common time axis to facilitate comparison with aerosol and sink measurements.

The combined particle number size distributions from NAIS and SMPS with sink parameters shows a temporal correspondence between particle population dynamics and sink strength. Periods with enhanced nucleation mode particle number concentrations in the NAIS spectrogram consistently coincide with reduced values of the CS. In contrast, days with persistently elevated sink values show no clear event-specific growth features in the nucleation mode part, indicating unfavourable conditions for the formation and growth in lower size range. To examine whether previously reported sink thresholds for polluted environments are consistent with observations at the CAS-AO, a horizontal reference line at 0.03 s^{-1} was included consistent with the event-day median CS reported in Section 3.2. When the sink strength drops below this level, particle number concentration enhancement in the nucleation and Aitken modes are observed. A pronounced example of this behaviour is observed on 7 October 2023, when particle growth initiates at approximately 3–4 nm (signals below this size are weak; however, the subsequent continuous growth suggests the presence of smaller clusters). Throughout the active NPF period on 7 October 2023, the condensation sink remains largely below ~0.03 s^{-1}. On the other days, CS also drops below this threshold transiently with correspondingly weak particle signals visible in the heatmap. A higher threshold of ~0.06 s⁻¹ has been reported for polluted urban environments such as Delhi (Ali et al., 2025), consistent with the behaviour observed here. In contrast, cleaner environment such as Helsinki typically show NPF at CS values of 0.01–0.03 s⁻¹, and remote sites at <0.01 s⁻¹ (Baranizadeh et al., 2017; Kulmala et al., 2013; Manninen et al., 2010). The relatively high-end threshold observed here suggests the strong sources of vapours that form clusters and grow them fast enough for maintaining high enough survival probability. 8 and 9 Oct show disrupted episodic high particle number concentration patches in 3–10 nm size range (in Fig. 11), likely due to variable meteorological conditions that disrupt sustained nucleation and growth. Corresponding meteorological data show variability in wind fields and radiation intensity, along with less coherent diurnal patterns for these other days. CS with meteorological variability can together possibly disrupt the balance between vapour production and particle losses, leading to fragmented or suppressed nucleation signatures. This may be case that clear NPF signatures at the CAS-AO occur under a combination of reduced sink conditions and favourable meteorological parameters, particularly wind and temperature.

To place observations from the CAS-AO in a broader urban pollution context, the CS values obtained in this study are interpreted alongside reported environmental ranges and process-based thresholds governing NPF. As established in Section 3.2, event-day CS (median 0.024 s⁻¹) is approximately half that of non-event days (0.046 s⁻¹), indicating a pronounced reduction in vapour scavenging during periods of particle formation. This reduction enhances the survival probability of freshly nucleated clusters by increasing vapour lifetime and reducing coagulation losses.

Reported values from polluted urban environments, such as those presented by (Gani et al., 2020; Laakso et al., 2006), span a wide range depending on pollution level and time of day, with CS values reaching ~0.14–0.17 s⁻¹ under highly polluted winter evening conditions, ~0.035 s⁻¹ during relatively cleaner spring daytime periods, and as low as ~0.004 s⁻¹ during monsoon afternoons. In this framework, the CAS-AO site represents an intermediate regime: event-day CS values (~0.024 s⁻¹) are comparable to cleaner urban daytime conditions, while non-event values (~0.046 s⁻¹) approach moderately polluted regimes.

Further observations from Delhi show that NPF events are typically observed when CS remains below ~0.06 s⁻¹, despite an overall range of ~0.004–0.8 s⁻¹, indicating that only periods with sufficiently reduced sink conditions allow particle formation and sustained growth (Ali et al., 2025). The event-day CS values in this study fall well within this favourable regime, whereas non-event conditions approach this threshold, indicating a transition between conditions that permit and inhibit NPF.

Importantly, the growth rates in this study exhibit a clear size dependence, increasing from ~9.7–11.4 nm h⁻¹ in the 3–7 nm range to ~12.9–15.6 nm h⁻¹ in the 7–20 nm range, indicating enhanced condensational growth at larger particle sizes. These values are comparable to the range of 5.7–30 nm h⁻¹ reported for Delhi in previous studies under highly polluted conditions (Ali et al., 2025; Mönkkönen et al., 2005; Sarangi et al., 2015). This suggests that while condensational growth can be efficient, particularly at larger sizes, the ability of particles to survive the initial growth stages remains strongly dependent on sink conditions.

The elevated CS reported for Delhi provides a mechanistic explanation for the frequent suppression of banana-shaped growth signatures in polluted urban conditions. While nucleation may still occur intermittently, the combined effect of rapid vapour removal and efficient particle scavenging strongly limits particle survival and growth. In contrast, the comparatively lower sink environment at Sonipat permits temporal windows favourable for particle survival and intermittent growth under suitable meteorological conditions.

4. Conclusion

This study presents the first systematic characterisation of size-resolved atmospheric ions and sub–10 nm particles at a suburban Indo-Gangetic Plain site (CAS-AO, Sonipat), combining NAIS and SMPS measurements with meteorological observations over May–December 2023 to examine the occurrence, microphysical characteristics, and governing conditions of new particle formation (NPF) in a high-pollution continental environment. Three complementary classification frameworks were applied to identify NPF events and compare their frequency and intensity across the observational period.

NPF events occurred predominantly during summer, exceeding 85 % of available days in May and June, while non-event conditions dominated in November and December (>85 % of days). Atmospheric ions in the 2–4 nm range showed modest diurnal enhancement (day/night ratio ~1.5–2.5), substantially weaker than the robust daytime increase in 3–5 nm particles (day/night ratio ~3–3.5 during summer). Presence of significant transported event-days (upto 30 %) with this number concentration decoupling indicates that neutral cluster pathways, rather than free ion abundance, govern nucleation-mode particle production at this site. Particle growth rates increased systematically with size, from median values of 10.6 (appearance time method) and 14.7 nm h^{-1} (maximum concentration method) in the 3–7 nm range to 16.8 (appearance time method) and 19.0 nm h^{-1} (maximum concentration method) in the 7–20 nm range, placing the IGP within the upper envelope of urban and polluted regional environments globally. Particle formation rates at 7 nm (J_7), determined for three days, were in the range of 50–60 cm^{-3} s^{-1} and at 3 nm, J_3 for only one possible day for which it could be estimated reliably was 81 cm^{-3} s^{-1}. event-days were characterised by condensation sinks (median: 0.024 s^{-1}, IQR: 0.016–0.033 s^{-1}) approximately half those on non-event days (0.046 s^{-1}, IQR: 0.034–0.062 s^{-1}), confirming that a sufficiently reduced scavenging environment is a necessary, though not independently sufficient, condition for NPF occurrence.

The event-day condensation sink at CAS-AO (0.024 s^{-1}) falls between the suppression thresholds reported for other polluted environments like Delhi and Beijing, and substantially above the typical range of clean environments such as the boreal forest (~10^{-3}–10^{-2} s^{-1}). This positions this site as an intermediate-pollution regime where NPF operates near the upper boundary of conditions permissive for cluster survival. The elevated growth rates observed here, particularly at larger particle sizes (7 to 20 nm), are consistent with the high condensable vapour concentrations expected in the anthropogenically influenced IGP boundary layer and are comparable to the 5.7–30 nm h^{-1} range reported for Delhi under similarly polluted conditions.

In this environment, however, pollution plumes, boundary layer variability, wind fluctuations, and precipitation intermittently mask or distort NPF signals introducing additional particle modes that overlap with or completely suppress the growing nucleation mode. As a result, both traditional visual classification methods and automated approaches, which were developed for cleaner environments with distinct lognormal size distributions, cannot be directly applied without careful adaptation.

Growth rate estimation methods similarly assume steady-state, size-independent growth and distinct modes assumptions frequently violated here. Preprocessing and smoothing procedures, while necessary to reduce noise, risk attenuating genuine atmospheric features or retaining artefacts where signal-to-noise ratios are low. Careful day-by-day screening remained necessary even when automated frameworks were applied, and quantitative parameters such as J and GR carry increased uncertainty relative to cleaner-site applications. These methodological limitations must be explicitly acknowledged in any interpretation of NPF characteristics in such environments.

Despite these limitations, the results collectively demonstrate that NPF makes a meaningful contribution to particle number in the IGP, with the relatively high growth rates, significant formation rates, and frequent summer occurrence suggesting a substantial secondary aerosol source with potential implications for regional CCN populations and cloud properties. While this study does not explicitly quantify the contribution of NPF to total particle number concentrations, the frequent occurrence of NPF events during summer likely represents a significant, possibly dominant, contribution to elevated particle number concentrations relative to background conditions. However, this association cannot be interpreted as a direct or causal enhancement of particle number concentrations by NPF, as multiple primary and secondary sources contribute simultaneously. In such conditions, isolating the fraction of particle number concentrations attributable solely to NPF requires rigorous separation of overlapping signals from local emissions, transported plumes, and background aerosol which remains a non-trivial challenge and addressing that explicitly is itself a motivation of the present study. The observed dominance of neutral over ion-induced pathways, and the strong control exerted by condensation sink on NPF occurrence, point to the need for integrated measurements combining sub–10 nm size distributions with precursor gas concentrations (particularly H_2SO_4, amines, and low-volatility organics) to constrain the nucleation mechanism. More broadly, this study underscores that advancing understanding of NPF in heavily polluted continental regions requires not only extended observational datasets but also the development of classification and parameter estimation methodologies explicitly designed for multi-source, high-condensation-sink environments where the assumptions underlying existing tools systematically break down.

Code and data availability

The observational data from the CAS-AO atmospheric observatory (NAIS ion and total particle number size distributions, SMPS particle size distributions, and AWS meteorological parameters) used in this study, together with the analysis codes will be made publicly available upon acceptance of this manuscript. The dataset and code repository will be archived at Zenodo [to be confirmed upon publication] and accessible via a persistent DOI that will be provided in the final published version of this article. Readers interested in accessing the data or code prior to publication are encouraged to contact the corresponding authors.

Author contributions

GKS and SG conceptualized the study. GKS, AAW, and JR carried out the data collection. GKS and JL curated the data. GKS developed the methodology and performed the formal analysis, visualization, and wrote the original draft of the manuscript. RKK, DG, MK, TP, PP, RCT, and SG provided resources. PP, RCT, and SG acquired funding, administered the project, and supervised the work. All authors contributed to reviewing and editing the manuscript.

Competing interests

The authors declare that they have no conflict of interest. TP is a member of the editorial board of ACP.

Acknowledgements

We would like to sincerely acknowledge Prof. Krishna Achuta Rao and Prof. Somnath Baidya Roy for their vision, leadership, and active involvement in the planning and administrative efforts that led to the establishment of the atmospheric observatory at IIT Delhi. We are also grateful to the senior administration of IIT Delhi for their continued support in building and sustaining this important scientific infrastructure. Special thanks to the Institute for Atmospheric and Earth System Research (INAR), University of Helsinki, for their collaboration and support in facilitating this research, particularly through the provision of instrumentation, technical guidance, and associated infrastructure that made key observations and analyses possible. ChatGPT (OpenAI) was used to assist with grammar, sentence structure, and language clarity during manuscript preparation. All scientific content, analysis, and interpretation were developed by the authors.

Financial support

We acknowledge financial support from the European Commission via FOCI Project (101056783), from the Research Council of Finland via Atmosphere and Climate Competence Centre (ACCC) Flagship (337549, 3570902, 359340) and via CO-ENHANCIN project (360114), Jane and Aatos Erkko Foundation and from University of Helsinki, Faculty of Science via ACTRIS-HY.

References

Aalto, P., Härmeri, K., Becker, E. D. O., Weber, R., Salm, J., Mäkelä, J. M., Hoell, C., O'dowd, C. D., Hansson, H.-C., Väkevä, M., and others: Physical characterization of aerosol particles during nucleation events, Tellus B: Chemical and Physical Meteorology, 53, 344–358, https://doi.org/10.1034/j.1600-0889.2001.530404.x, 2001.

Aalto, P., Hämeri, K., Becker, E., Weber, R., Salm, J., Mäkelä, J. M., Hoell, C., O'dowd, C. D., Karlsson, H., Hansson, H.-C., Väkevä, M., Koponen, I. K., Buzorius, G., and Kulmala, M.: Physical characterization of aerosol particles during nucleation events, Tellus B Chem. Phys. Meteorol., 53, 344, https://doi.org/10.3402/tellusb.v53i4.17127, 2001.

Ali, U., Singh, V., Faisal, M., Kumar, M., and Gani, S.: Exploring the influence of physical and chemical factors on new particle formation in a polluted megacity, Environ. Sci. Atmospheres, 5, 25–47, https://doi.org/10.1039/d4ea00114a, 2025.

Aliaga, D., Tuovinen, S., Zhang, T., Lampilahti, J., Li, X., Ahonen, L., Kokkonen, T., Nieminen, T., Hakala, S., Paasonen, P., Bianchi, F., Worsnop, D., Kerminen, V.-M., and Kulmala, M.: Nanoparticle ranking analysis: determining new particle formation (NPF) event occurrence and intensity based on the concentration spectrum of formed (sub-5 nm) particles, Aerosol Res., 1, 81–92, https://doi.org/10.5194/ar-1-81-2023, 2023.

Asmi, E., Kivekäs, N., Kerminen, V.-M., Komppula, M., Hyvärinen, A.-P., Hatakka, J., Viisanen, Y., and Lihavainen, H.: Secondary new particle formation in Northern Finland Pallas site between the years 2000 and 2010, Atmospheric Chem. Phys., 11, 12959–12972, https://doi.org/10.5194/acp-11-12959-2011, 2011.

Baranizadeh, E., Nieminen, T., Yli-Juuti, T., Kulmala, M., Petäjä, T., Leskinen, A., Komppula, M., Laaksonen, A., and Lehtinen, K. E. J.: Estimation of atmospheric particle formation rates through an analytical formula: validation and application in Hyytiälä and Puijo, Finland, Atmospheric Chem. Phys., 17, 13361–13371, https://doi.org/10.5194/acp-17-13361-2017, 2017.

Bazilevskaya, G. A., Usoskin, I. G., Flückiger, E. O., Harrison, R. G., Desorgher, L., Bütikofer, R., Krainev, M. B., Makhmutov, V. S., Stozhkov, Y. I., Svirzhevskaya, A. K., Svirzhevsky, N. S., and Kovaltsov, G. A.: Cosmic Ray Induced Ion Production in the Atmosphere, Space Sci. Rev., 137, 149–173, https://doi.org/10.1007/s11214-008-9339-y, 2008.

Boy, M., Kazil, J., Lovejoy, E. R., Guenther, A., and Kulmala, M.: Relevance of ion-induced nucleation of sulfuric acid and water in the lower troposphere over the boreal forest at northern latitudes, Atmospheric Res., 90, 151–158, https://doi.org/10.1016/j.atmosres.2008.01.002, 2008.

Cai, R., Yan, C., Yang, D., Yin, R., Lu, Y., Deng, C., Fu, Y., Ruan, J., Li, X., Kontkanen, J., Zhang, Q., Kangasluoma, J., Ma, Y., Hao, J., Worsnop, D. R., Bianchi, F., Paasonen, P., Kerminen, V.-M., Liu, Y., Wang, L., Zheng, J., Kulmala, M., and Jiang, J.: Sulfuric acid–amine nucleation in urban Beijing, Atmospheric Chem. Phys., 21, 2457–2468, https://doi.org/10.5194/acp-21-2457-2021, 2021.

Carslaw, K. S., Harrison, R. G., and Kirkby, J.: Cosmic Rays, Clouds, and Climate, Science, 298, 1732–1737, https://doi.org/10.1126/science.1076964, 2002.

Chutia, L., Ojha, N., Girach, I., Pathak, B., Sahu, L. K., Sarangi, C., Flemming, J., Da Silva, A., and Bhuyan, P. K.: Trends in sulfur dioxide over the Indian subcontinent during 2003–2019, Atmos. Environ., 284, 119189, https://doi.org/10.1016/j.atmosenv.2022.119189, 2022.

CIMO Guide No.8, WMO,: Guide to Meteorological Instruments and Methods of Observation: (CIMO guide). 2014 edition, updated in 2017.[SUPERSEDED], https://doi.org/10.25607/OBP-432, 2017.

Dada, L., Chellapermal, R., Buenrostro Mazon, S., Paasonen, P., Lampilahti, J., Manninen, H. E., Junninen, H., Petäjä, T., Kerminen, V.-M., and Kulmala, M.: Refined classification and characterization of atmospheric new-particle formation events using air ions, Atmospheric Chem. Phys., 18, 17883–17893, https://doi.org/10.5194/acp-18-17883-2018, 2018.

Deng, C., Cai, R., Yan, C., Zheng, J., and Jiang, J.: Formation and growth of sub-3 nm particles in megacities: impact of background aerosols, Faraday Discuss., 226, 348–363, https://doi.org/10.1039/D0FD00083C, 2021.

Eisenbud, M. and Gesell, T. F.: Environmental radioactivity: from natural, industrial, and military sources, 4th ed., Academic Press, San Diego, 1997.

Gani, S., Bhandari, S., Seraj, S., Wang, D. S., Patel, K., Soni, P., Arub, Z., Habib, G., Hildebrandt Ruiz, L., and Apte, J. S.: Submicron aerosol composition in the world's most polluted megacity: the Delhi Aerosol Supersite study, Atmospheric Chem. Phys., 19, 6843–6859, https://doi.org/10.5194/acp-19-6843-2019, 2019.

Gani, S., Bhandari, S., Patel, K., Seraj, S., Soni, P., Arub, Z., Habib, G., Hildebrandt Ruiz, L., and Apte, J. S.: Particle number concentrations and size distribution in a polluted megacity: the Delhi Aerosol Supersite study, Atmospheric Chem. Phys., 20, 8533–8549, https://doi.org/10.5194/acp-20-8533-2020, 2020.

Guttikunda, S. K. and Gurjar, B. R.: Role of meteorology in seasonality of air pollution in megacity Delhi, India, Environ. Monit. Assess., 184, 3199–3211, https://doi.org/10.1007/s10661-011-2182-8, 2012.

Herrmann, E., Ding, A. J., Kerminen, V.-M., Petäjä, T., Yang, X. Q., Sun, J. N., Qi, X. M., Manninen, H., Hakala, J., Nieminen, T., Aalto, P. P., Kulmala, M., and Fu, C. B.: Aerosols and nucleation in eastern China: first insights from the new SORPES-NJU station, Atmospheric Chem. Phys., 14, 2169–2183, https://doi.org/10.5194/acp-14-2169-2014, 2014.

Hinds, W. C. and Zhu, Y.: Aerosol technology: properties, behavior, and measurement of airborne particles, Third edition., Wiley, Hoboken, NJ, 425 pp., 2022.

Iida, K., Stolzenburg, M. R., McMurry, P. H., and Smith, J. N.: Estimating nanoparticle growth rates from size-dependent charged fractions: Analysis of new particle formation events in Mexico City, J. Geophys. Res. Atmospheres, 113, 2007JD009260, https://doi.org/10.1029/2007JD009260, 2008.

Johnson, T. J., Nishida, R. T., Irwin, M., Symonds, J. P. R., Olfert, J. S., and Boies, A. M.: Measuring the bipolar charge distribution of nanoparticles: Review of methodologies and development using the Aerodynamic Aerosol Classifier, J. Aerosol Sci., 143, 105526, https://doi.org/10.1016/j.jaerosci.2020.105526, 2020.

Kanawade, V. P., Sebastian, M., Hooda, R. K., and Hyvärinen, A.-P.: Atmospheric new particle formation in India: Current understanding and knowledge gaps, Atmos. Environ., 270, 118894, https://doi.org/10.1016/j.atmosenv.2021.118894, 2022.

Kangasluoma, J., Cai, R., Jiang, J., Deng, C., Stolzenburg, D., Ahonen, L. R., Chan, T., Fu, Y., Kim, C., Laurila, T. M., Zhou, Y., Dada, L., Sulo, J., Flagan, R. C., Kulmala, M., Petäjä, T., and Lehtipalo, K.: Overview of measurements and current instrumentation for 1–10 nm aerosol particle number size distributions, J. Aerosol Sci., 148, 105584, https://doi.org/10.1016/j.jaerosci.2020.105584, 2020.

Kerminen, V.-M., Chen, X., Vakkari, V., Petäjä, T., Kulmala, M., and Bianchi, F.: Atmospheric new particle formation and growth: review of field observations, Environ. Res. Lett., 13, 103003, https://doi.org/10.1088/1748-9326/aadf3c, 2018.

Kirkby, J., Duplissy, J., Sengupta, K., Frege, C., Gordon, H., Williamson, C., Heinritzi, M., Simon, M., Yan, C., Almeida, J., Tröstl, J., Nieminen, T., Ortega, I. K., Wagner, R., Adamov, A., Amorim, A., Bernhammer, A.-K., Bianchi, F., Breitenlechner, M., Brilke, S., Chen, X., Craven, J., Dias, A., Ehrhart, S., Flagan, R. C., Franchin, A., Fuchs, C., Guida, R., Hakala, J., Hoyle,

C. R., Jokinen, T., Junninen, H., Kangasluoma, J., Kim, J., Krapf, M., Kürten, A., Laaksonen, A., Lehtipalo, K., Makhmutov, V., Mathot, S., Molteni, U., Onnela, A., Peräkylä, O., Piel, F., Petäjä, T., Praplan, A. P., Pringle, K., Rap, A., Richards, N. A. D., Riipinen, I., Rissanen, M. P., Rondo, L., Sarnela, N., Schobesberger, S., Scott, C. E., Seinfeld, J. H., Sipilä, M., Steiner, G., Stozhkov, Y., Stratmann, F., Tomé, A., Virtanen, A., Vogel, A. L., Wagner, A. C., Wagner, P. E., Weingartner, E., Wimmer, D., Winkler, P. M., Ye, P., Zhang, X., Hansel, A., Dommen, J., Donahue, N. M., Worsnop, D. R., Baltensperger, U., Kulmala, M., Carslaw, K. S., and Curtius, J.: Ion-induced nucleation of pure biogenic particles, Nature, 533, 521–526, https://doi.org/10.1038/nature17953, 2016.

Kontkanen, J., Järvinen, E., Manninen, H. E., Lehtipalo, K., Kangasluoma, J., Decesari, S., Gobbi, G. P., Laaksonen, A., Petäjä, T., and Kulmala, M.: High concentrations of sub-3nm clusters and frequent new particle formation observed in the Po Valley, Italy, during the PEGASOS 2012 campaign, Atmospheric Chem. Phys., 16, 1919–1935, https://doi.org/10.5194/acp-16-1919-2016, 2016.

Kulmala, M. and Laaksonen, A.: Binary nucleation of water–sulfuric acid system: Comparison of classical theories with different H2SO4 saturation vapor pressures, J. Chem. Phys., 93, 696–701, https://doi.org/10.1063/1.459519, 1990.

Kulmala, M., Laakso, L., Lehtinen, K. E. J., Riipinen, I., Dal Maso, M., Anttila, T., Kerminen, V.-M., Hõrrak, U., Vana, M., and Tammet, H.: Initial steps of aerosol growth, Atmospheric Chem. Phys., 4, 2553–2560, https://doi.org/10.5194/acp-4-2553-2004, 2004.

Kulmala, M., Riipinen, I., Sipilä, M., Manninen, H. E., Petäjä, T., Junninen, H., Maso, M. D., Mordas, G., Mirme, A., Vana, M., Hirsikko, A., Laakso, L., Harrison, R. M., Hanson, I., Leung, C., Lehtinen, K. E. J., and Kerminen, V.-M.: Toward Direct Measurement of Atmospheric Nucleation, Science, 318, 89–92, https://doi.org/10.1126/science.1144124, 2007.

Kulmala, M., Petäjä, T., Nieminen, T., Sipilä, M., Manninen, H. E., Lehtipalo, K., Dal Maso, M., Aalto, P. P., Junninen, H., Paasonen, P., Riipinen, I., Lehtinen, K. E. J., Laaksonen, A., and Kerminen, V.-M.: Measurement of the nucleation of atmospheric aerosol particles, Nat. Protoc., 7, 1651–1667, https://doi.org/10.1038/nprot.2012.091, 2012.

Kulmala, M., Kontkanen, J., Junninen, H., Lehtipalo, K., Manninen, H. E., Nieminen, T., Petäjä, T., Sipilä, M., Schobesberger, S., Rantala, P., Franchin, A., Jokinen, T., Järvinen, E., Äijälä, M., Kangasluoma, J., Hakala, J., Aalto, P. P., Paasonen, P., Mikkilä, J., Vanhanen, J., Aalto, J., Hakola, H., Makkonen, U., Ruuskanen, T., Mauldin, R. L., Duplissy, J., Vehkamäki, H., Bäck, J., Kortelainen, A., Riipinen, I., Kurtén, T., Johnston, M. V., Smith, J. N., Ehn, M., Mentel, T. F., Lehtinen, K. E. J., Laaksonen, A., Kerminen, V.-M., and Worsnop, D. R.: Direct Observations of Atmospheric Aerosol Nucleation, Science, 339, 943–946, https://doi.org/10.1126/science.1227385, 2013.

Kulmala, M., Kerminen, V.-M., Petäjä, T., Ding, A. J., and Wang, L.: Atmospheric gas-to-particle conversion: why NPF events are observed in megacities?, Faraday Discuss., 200, 271–288, https://doi.org/10.1039/C6FD00257A, 2017.

Kulmala, M., Junninen, H., Dada, L., Salma, I., Weidinger, T., Thén, W., Vörösmarty, M., Komsaare, K., Stolzenburg, D., Cai, R., Yan, C., Li, X., Deng, C., Jiang, J., Petäjä, T., Nieminen, T., and Kerminen, V.-M.: Quiet New Particle Formation in the Atmosphere, Front. Environ. Sci., 10, 912385, https://doi.org/10.3389/fenvs.2022.912385, 2022.

Kulmala, M., Aliaga, D., Tuovinen, S., Cai, R., Junninen, H., Yan, C., Bianchi, F., Cheng, Y., Ding, A., Worsnop, D. R., Petäjä, T., Lehtipalo, K., Paasonen, P., and Kerminen, V.-M.: Opinion: A paradigm shift in investigating the general characteristics of atmospheric new particle formation using field observations, Aerosol Res., 2, 49–58, https://doi.org/10.5194/ar-2-49-2024, 2024.

Laakso, L.: Ultrafine particle scavenging coefficients calculated from 6 years field measurements, Atmos. Environ., 37, 3605–3613, https://doi.org/10.1016/S1352-2310(03)00326-1, 2003.

Laakso, L., Koponen, I. K., Mönkkönen, P., Kulmala, M., Kerminen, V.-M., Wehner, B., Wiedensohler, A., Wu, Z., and Hu, M.: Aerosol particles in the developing world; a comparison between New Delhi in India and Beijing in China, Water. Air. Soil Pollut., 173, 5–20, https://doi.org/10.1007/s11270-005-9018-5, 2006.

Lampilahti, J., Paasonen, P., Tuovinen, S., Lehtipalo, K., Kerminen, V.-M., and Kulmala, M.: A cross-correlation-based method for determining size-resolved particle growth rates, Aerosol Res., 3, 637–647, https://doi.org/10.5194/ar-3-637-2025, 2025.

Lehtipalo, K., Leppä, J., Kontkanen, J., Kangasluoma, J., Franchin, A., Wimmer, D., Schobesberger, S., Junninen, H., Petäjä, T., Sipilä, M., Mikkilä, J., Vanhanen, J., Worsnop, D. R., and Kulmala, M.: Methods for determining particle size distribution and growth rates between 1 and 3 nm using the Particle Size Magnifier, Boreal Environ. Res., 19, 22, 2014.

Leppä, J., Mui, W., Grantz, A. M., and Flagan, R. C.: Charge distribution uncertainty in differential mobility analysis of aerosols, Aerosol Sci. Technol., 51, 1168–1189, https://doi.org/10.1080/02786826.2017.1341039, 2017.

Manninen, H. E., Nieminen, T., Asmi, E., Gagné, S., Häkkinen, S., Lehtipalo, K., Aalto, P., Vana, M., Mirme, A., Mirme, S., Hõrrak, U., Plass-Dülmer, C., Stange, G., Kiss, G., Hoffer, A., Törő, N., Moerman, M., Henzing, B., De Leeuw, G., Brinkenberg, M., Kouvarakis, G. N., Bougiatioti, A., Mihalopoulos, N., O'Dowd, C., Ceburnis, D., Arneth, A., Svenningsson, B., Swietlicki, E., Tarozzi, L., Decesari, S., Facchini, M. C., Birmili, W., Sonntag, A., Wiedensohler, A., Boulon, J., Sellegri, K., Laj, P., Gysel, M., Bukowiecki, N., Weingartner, E., Wehrle, G., Laaksonen, A., Hamed, A., Joutsensaari, J., Petäjä, T., Kerminen, V.-M., and Kulmala, M.: EUCAARI ion spectrometer measurements at 12 European sites – analysis of new particle formation events, Atmospheric Chem. Phys., 10, 7907–7927, https://doi.org/10.5194/acp-10-7907-2010, 2010.

Manninen, H. E., Franchin, A., Schobesberger, S., Hirsikko, A., Hakala, J., Skromulis, A., Kangasluoma, J., Ehn, M., Junninen, H., Mirme, A., Mirme, S., Sipilä, M., Petäjä, T., Worsnop, D. R., and Kulmala, M.: Characterisation of corona-generated ions used in a Neutral cluster and Air Ion Spectrometer (NAIS), Atmospheric Meas. Tech., 4, 2767–2776, https://doi.org/10.5194/amt-4-2767-2011, 2011.

Mirme, S. and Mirme, A.: The mathematical principles and design of the NAIS – a spectrometer for the measurement of cluster ion and nanometer aerosol size distributions, Atmospheric Meas. Tech., 6, 1061–1071, https://doi.org/10.5194/amt-6-1061-2013, 2013.

Mironova, I. A., Aplin, K. L., Arnold, F., Bazilevskaya, G. A., Harrison, R. G., Krivolutsky, A. A., Nicoll, K. A., Rozanov, E. V., Turunen, E., and Usoskin, I. G.: Energetic Particle Influence on the Earth's Atmosphere, Space Sci. Rev., 194, 1–96, https://doi.org/10.1007/s11214-015-0185-4, 2015.

Mönkkönen, P., Koponen, I. K., Lehtinen, K. E. J., Hämeri, K., Uma, R., and Kulmala, M.: Measurements in a highly polluted Asian mega city: observations of aerosol number size distribution, modal parameters and nucleation events, Atmospheric Chem. Phys., 5, 57–66, https://doi.org/10.5194/acp-5-57-2005, 2005.

Paasonen, P., Peltola, M., Kontkanen, J., Junninen, H., Kerminen, V.-M., and Kulmala, M.: Comprehensive analysis of particle growth rates from nucleation mode to cloud condensation nuclei in boreal forest, Atmospheric Chem. Phys., 18, 12085–12103, https://doi.org/10.5194/acp-18-12085-2018, 2018.

Pawar, P. V., Ghude, S. D., Govardhan, G., Acharja, P., Kulkarni, R., Kumar, R., Sinha, B., Sinha, V., Jena, C., Gunwani, P., Adhya, T. K., Nemitz, E., and Sutton, M. A.: Chloride (HCl/Cl^-) dominates inorganic aerosol formation from ammonia in the Indo-Gangetic Plain during winter: modeling and comparison with observations, Atmospheric Chem. Phys., 23, 41–59, https://doi.org/10.5194/acp-23-41-2023, 2023.

Rathore, J., Ganguly, D., Singh, V., Gupta, M., Vazhathara, V. J., Biswal, A., Kunchala, R. K., Patra, P. K., Sahu, L. K., Gani, S., and Dey, S.: Characteristics of Haze Pollution Events During Biomass Burning Period at an Upwind Site of Delhi, J. Geophys. Res. Atmospheres, 130, e2024JD042347, https://doi.org/10.1029/2024JD042347, 2025.

Sarangi, B., Aggarwal, S. G., and Gupta, P. K.: A Simplified Approach to Calculate Particle Growth Rate Due to Self-Coagulation, Scavenging and Condensation Using SMPS Measurements during a Particle Growth Event in New Delhi, Aerosol Air Qual. Res., 15, 166–179, https://doi.org/10.4209/aaqr.2013.12.0350, 2015.

Sebastian, M., Kompalli, S. K., Kumar, V. A., Jose, S., Babu, S. S., Pandithurai, G., Singh, S., Hooda, R. K., Soni, V. K., Pierce, J. R., Vakkari, V., Asmi, E., Westervelt, D. M., Hyvärinen, A.-P., and Kanawade, V. P.: Observations of particle number size distributions and new particle formation in six Indian locations, Atmospheric Chem. Phys., 22, 4491–4508, https://doi.org/10.5194/acp-22-4491-2022, 2022.

Seinfeld, J. H. and Pandis, S. N.: Atmospheric chemistry and physics: from air pollution to climate change, 2nd ed., J. Wiley, Hoboken, N.J, 1203 pp., 2016.

Sellegri, K., Rose, C., Marinoni, A., Lupi, A., Wiedensohler, A., Andrade, M., Bonasoni, P., and Laj, P.: New Particle Formation: A Review of Ground-Based Observations at Mountain Research Stations, Atmosphere, 10, 493, https://doi.org/10.3390/atmos10090493, 2019.

Singh, N., Dey, S., and Knibbs, L. D.: Spatio-temporal patterns of tropospheric NO2 over India during 2005–2019, Atmospheric Pollut. Res., 14, 101692, https://doi.org/10.1016/j.apr.2023.101692, 2023.

Spracklen, D. V., Carslaw, K. S., Merikanto, J., Mann, G. W., Reddington, C. L., Pickering, S., Ogren, J. A., Andrews, E., Baltensperger, U., Weingartner, E., Boy, M., Kulmala, M., Laakso, L., Lihavainen, H., Kivekäs, N., Komppula, M., Mihalopoulos, N., Kouvarakis, G., Jennings, S. G., O'Dowd, C., Birmili, W., Wiedensohler, A., Weller, R., Gras, J., Laj, P., Sellegri, K., Bonn, B., Krejci, R., Laaksonen, A., Hamed, A., Minikin, A., Harrison, R. M., Talbot, R., and Sun, J.: Explaining global surface aerosol number concentrations in terms of primary emissions and particle formation, Atmospheric Chem. Phys., 10, 4775–4793, https://doi.org/10.5194/acp-10-4775-2010, 2010.

Stolzenburg, D., Cai, R., Blichner, S. M., Kontkanen, J., Zhou, P., Makkonen, R., Kerminen, V.-M., Kulmala, M., Riipinen, I., and Kangasluoma, J.: Atmospheric nanoparticle growth, Rev. Mod. Phys., 95, 045002, https://doi.org/10.1103/RevModPhys.95.045002, 2023.

Stolzenburg, M. R. and McMurry, P. H.: Method to assess performance of scanning mobility particle sizer (SMPS) instruments and software, Aerosol Sci. Technol., 52, 609–613, https://doi.org/10.1080/02786826.2018.1455962, 2018.

Tammet, H.: Size and mobility of nanometer particles, clusters and ions, J. Aerosol Sci., 26, 459–475, https://doi.org/10.1016/0021-8502(94)00121-E, 1995.

Tomasi, C. and Lupi, A.: Primary and Secondary Sources of Atmospheric Aerosol, in: Atmospheric Aerosols, edited by: Tomasi, C., Fuzzi, S., and Kokhanovsky, A., Wiley, 1–86, https://doi.org/10.1002/9783527336449.ch1, 2017.

Trivedi, D. K., Ali, K., and Beig, G.: Impact of meteorological parameters on the development of fine and coarse particles over Delhi, Sci. Total Environ., 478, 175–183, https://doi.org/10.1016/j.scitotenv.2014.01.101, 2014.

Wagner, R., Manninen, H. E., Franchin, A., Lehtipalo, K., Mirme, S., Steiner, G., Petäjä, T., and Kulmala, M.: On the accuracy of ion measurements using a neutral cluster and air ion spectrometer, BOREAL Environ. Res., 21, 230–241, https://doi.org/10.60910/XR8J-5A1A, 2016.

Wang, T., Song, Y., Xu, Z., Liu, M., Xu, T., Liao, W., Yin, L., Cai, X., Kang, L., Zhang, H., and Zhu, T.: Why is the Indo-Gangetic Plain the region with the largest NH_3 column in the globe during pre-monsoon and monsoon seasons?, Atmospheric Chem. Phys., 20, 8727–8736, https://doi.org/10.5194/acp-20-8727-2020, 2020.

Yli-Juuti, T., Nieminen, T., Hirsikko, A., Aalto, P. P., Asmi, E., Hõrrak, U., Manninen, H. E., Patokoski, J., Dal Maso, M., Petäjä, T., Rinne, J., Kulmala, M., and Riipinen, I.: Growth rates of nucleation mode particles in Hyytiälä during 2003−2009: variation with particle size, season, data analysis method and ambient conditions, Atmospheric Chem. Phys., 11, 12865–12886, https://doi.org/10.5194/acp-11-12865-2011, 2011.

Yu, F. and Turco, R. P.: From molecular clusters to nanoparticles: Role of ambient ionization in tropospheric aerosol formation, J. Geophys. Res. Atmospheres, 106, 4797–4814, https://doi.org/10.1029/2000JD900539, 2001.

Yu, M., Tang, G., Yang, Y., Li, Q., Wang, Y., Miao, S., Zhang, Y., and Wang, Y.: The interaction between urbanization and aerosols during a typical winter haze event in Beijing, Atmospheric Chem. Phys., 20, 9855–9870, https://doi.org/10.5194/acp-20-9855-2020, 2020.

Zhang, K., Xu, Z., Zhang, F., and Wang, Z.: Unveiling the organic contribution to the initial particle growth in 3–10 nm size range, Atmospheric Chem. Phys., 26, 2241–2254, https://doi.org/10.5194/acp-26-2241-2026, 2026.